Article

Cancer Cell

IDH2 and TET2 mutations synergize to modulate T Follicular Helper cell functional interaction with the AITL microenvironment

Graphical abstract

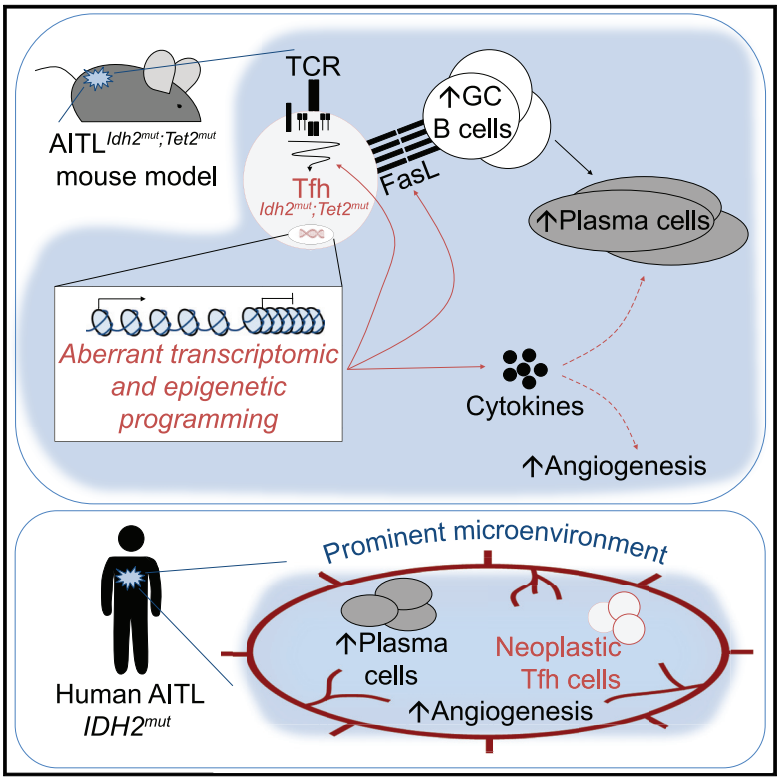

Highlights

- *Idh2*;*Tet2*-mutated T cells induce AITL after transplantation into recipient mice
- *Idh2*;*Tet2* mutations alter Tfh cell transcriptomics and epigenetics
- *Idh2*;*Tet2* mutations alter Tfh cell phenotype/function, normal B cells, and the TME
- Combined *Idh2*;*Tet2* mutation downregulates FasL signaling in Tfh cells

Authors

Julie Leca, François Lemonnier, Cem Meydan, ..., Ari Melnick, Philippe Gaulard, Tak W. Mak

Correspondence

julie.leca@uhnresearch.ca (J.L.), tak.mak@uhnresearch.ca (T.W.M.)

In brief

Leca et al. show that combining *Idh2* and *Tet2* mutations in mouse T cells leads to an AITL-like disease that recapitulates features of human AITL. These two mutations synergize at the transcriptomic and epigenetic levels to alter the functions of Tfh cells and their relationship with the tumor microenvironment.

Leca et al., 2023, Cancer Cell *41*, 323–339
February 13, 2023
https://doi.org/10.1016/j.ccell.2023.01.003

CellPress

Cancer Cell

CellPress
OPEN ACCESS

Article

IDH2 and TET2 mutations synergize to modulate T Follicular Helper cell functional interaction with the AITL microenvironment

Julie Leca,[1,*] François Lemonnier,[2,3] Cem Meydan,[4,5,15] Jonathan Foox,[4,5,15] Samah El Ghamrasni,[1] Diana-Laure Mboumba,[2] Gordon S. Duncan,[1] Jerome Fortin,[1] Takashi Sakamoto,[1,6] Chantal Tobin,[1] Kelsey Hodgson,[1] Jillian Haight,[1] Logan K. Smith,[1] Andrew J. Elia,[1] Daniel Butler,[4] Thorsten Berger,[1] Laurence de Leval,[7,8] Christopher E. Mason,[4,5,9] Ari Melnick,[10] Philippe Gaulard,[2,11] and Tak W. Mak[1,12,13,14,16,*]

[1]University Health Network, Princess Margaret Cancer Centre, Toronto, ON M5G 1L7, Canada
[2]University Paris-Est Créteil, INSERM U955, Institut Mondor de Recherche Biomédicale, 94010 Créteil, France
[3]AP-HP, Lymphoid Malignancies Unit, Henri Mondor Hospital, 94010 Créteil, France
[4]Department of Physiology and Biophysics, Weill Cornell Medicine, New York, NY 10021, USA
[5]The HRH Prince Alwaleed Bin Talal Bin Abdulaziz Alsaud Institute for Computational Biomedicine, Weill Cornell Medicine, New York, NY 10065, USA
[6]Department of Hematology and Oncology, Graduate School of Medicine, Kyoto University, Kyoto 606-8501, Japan
[7]Institute of Pathology, Department of Laboratory Medicine and Pathology, Lausanne University Hospital, Lausanne 1011, Switzerland
[8]Lausanne University, Lausanne 1011, Switzerland
[9]WorldQuant Initiative for Quantitative Prediction, Weill Cornell Medicine, New York, NY 10021, USA
[10]Department of Medicine, Division of Hematology and Medical Oncology, Weill Cornell Medicine, New York, NY 10065, USA
[11]AP-HP, Pathology Department, Henri Mondor Hosital, 94010 Créteil, France
[12]Departments of Medical Biophysics and Immunology, University of Toronto, Toronto, ON M5G 1L7, Canada
[13]Department of Pathology, School of Clinical Medicine, Li Ka Shing Faculty of Medicine, The University of Hong Kong, Hong Kong SAR, China
[14]Centre for Oncology and Immunology, Hong Kong Science Park, Hong Kong SAR, China
[15]These authors contributed equally
[16]Lead contact
*Correspondence: julie.leca@uhnresearch.ca (J.L.), tak.mak@uhnresearch.ca (T.W.M.)
https://doi.org/10.1016/j.ccell.2023.01.003

SUMMARY

Angioimmunoblastic T cell lymphoma (AITL) is a peripheral T cell lymphoma that originates from T follicular helper (Tfh) cells and exhibits a prominent tumor microenvironment (TME). *IDH2* and *TET2* mutations co-occur frequently in AITL, but their contribution to tumorigenesis is poorly understood. We developed an AITL mouse model that is driven by *Idh2* and *Tet2* mutations. Malignant Tfh cells display aberrant transcriptomic and epigenetic programs that impair TCR signaling. Neoplastic Tfh cells bearing combined *Idh2* and *Tet2* mutations show altered cross-talk with germinal center B cells that promotes B cell clonal expansion while decreasing Fas-FasL interaction and reducing B cell apoptosis. The plasma cell count and angiogenesis are also increased in the *Idh2*-mutated tumors, implying a major relationship between *Idh2* mutation and the characteristic AITL TME. Our mouse model recapitulates several features of human *IDH2*-mutated AITL and provides a rationale for exploring therapeutic targeting of Tfh-TME cross-talk for AITL patients.

INTRODUCTION

Angioimmunoblastic T cell lymphoma (AITL) is one of the most prevalent peripheral T cell lymphomas (PTCL). AITL patients are often resistant to chemotherapy and have poor clinical outcomes.[1] The cell of origin of AITL is the T follicular helper (Tfh) cell, a subtype of $CD4^+$ effector T cell that localizes in germinal centers (GC) and supports B cell responses.[2] The neoplastic cells in AITL exhibit a Tfh gene signature that includes expression of the chemokine receptors CXCR5 and CXCL13, programmed cell death-1 (PD-1), and inducible T cell co-stimulator (ICOS).[2,3]

In addition to neoplastic Tfh cells, AITL is characterized by an extensive tumor microenvironment (TME) composed mainly of reactive hematopoietic cells, including T and B cells, plasma cells, histiocytes, and eosinophils. This TME also contains stromal cells, including follicular dendritic cells (FDCs), and shows prominent arborization of high endothelial venules.[3] Interactions between TME components and cytokines released by neoplastic Tfh cells establish and maintain AITL pathology.[2] Cross-talk between

neoplastic Tfh cells and B cells in the AITL TME is vital for tumor progression, as demonstrated in various mouse models.[4,5] Moreover, a subset of AITL patients may develop prominent B cell expansion or occasionally an associated B cell lymphoma.[6,7]

At the genomic level, AITL features a relatively homogeneous mutational landscape in which ten-eleven translocation-2 (*TET2*) mutations occur in ~80% of patients,[8] and Ras homolog family member A (*RHOA*) mutations are found in 50%–70% of patients.[9,10] In addition, *DNMT3A*[11] and isocitrate dehydrogenase-2 (*IDH2*)[12] mutations are detected in 20%–30% of AITL patients. It is thought that AITL develops in steps, with *TET2* and *DNMT3A* mutations arising in hematopoietic progenitors and inducing clonal hematopoiesis, followed by "second hit" events such as *RHOA* and *IDH2* mutations that drive malignant transformation.[9] Indeed, combining *Tet2* and *RhoA* mutations in mouse models leads to AITL-like disease.[13–16]

The role of *IDH2* mutation in AITL is particularly intriguing. *IDH2*-mutated AITL almost always shows co-occurrence of a *TET2* mutation. However, how *IDH2* mutation contributes to AITL disease is poorly understood. *IDH* mutation confers neomorphic enzymatic activity that reduces α-ketoglutarate (αKG) to D-2-hydroxyglutarate (D2HG). D2HG can inhibit several dioxygenases that use αKG as a cofactor, including histone demethylases and TET proteins involved in DNA demethylation.[17,18] The *IDH2* mutations in AITL patients almost exclusively affect $IDH2^{R172}$, likely because only this alteration produces enough D2HG to have a biological effect in T cells.[19] *IDH2*-mutated AITL also shows bone marrow (BM) involvement, a cytological signature featuring medium-to-large clear tumor cells, elevated Tfh cell markers, an expanded FDC meshwork, and a distinctive gene expression pattern.[10,20,21] These findings suggest that mutant *IDH2*'s role in AITL may be related to its effects on the TME.

In this study, we use genetically engineered mouse models (GEMMs) and adoptive transfer (AT) mouse models to explore how *Tet2* and *Idh2* mutations cooperate in AITL pathogenesis. Through phenotypic, transcriptomic, and epigenomic analyses, we characterize the Tfh cells in these models and show how *Idh2* mutation enables Tfh cells to modulate the TME and drive AITL oncogenesis.

RESULTS

T cell-specific *Idh2* and *Tet2* mutations affect Tfh cells and GC B cells

To investigate the roles of $IDH2^{R172K}$ and *TET2* mutations in AITL, we first generated a GEMM combining a heterozygous Cre-inducible $Idh2^{LSL-R172K}$ knockin allele,[19] homozygous conditional $Tet2^{f/f}$ knockout alleles, and the *Cd4*-Cre driver. We compared these double-mutant mice ($Idh2^{LSL-R172K/+}$;$Tet2^{f/f}$;*Cd4*-Cre, designated [*Idh2*;*Tet2*]) with single-mutant $Idh2^{LSL-R172K/+}$;*Cd4*-Cre (*Idh2*) and $Tet2^{f/f}$;*Cd4*-Cre (*Tet2*) mice as well as with wild-type (WT) control *Cd4*-Cre mice. *Idh2*;*Tet2* mice displayed shorter survival than either *Idh2* or *Tet2* mice (Figure S1A). Intracellular D2HG levels were higher in $CD3^+$ T cells isolated from *Idh2*;*Tet2* mice compared with those from *Idh2* mice (Figure S1B). There were no differences in thymic subpopulations or total $CD3^+$ T cell numbers, but the double mutation led to decreased $CD4^+$ and $CD8^+$ naive T cells and increased $CD4^+$ and $CD8^+$ memory cells in the spleen (Figures S1C–S1F).

Idh2;*Tet2* mice showed an increased proportion of splenic $CD4^+CXCR5^+PD\text{-}1^+$ T cells expressing ICOS, suggesting Tfh cell expansion, as well as a higher percentage of GC B cells (Figures S1G and S1H). However, moribund *Idh2*;*Tet2* mice displayed prominent infiltration of $CD11b^+$ myeloid cells in the spleen, many of which were immature based on their cKit expression (Figure S1I). This apparent myeloid development was surprising given our use of the supposedly T cell-restricted *Cd4-Cre* driver. Therefore, we crossed *Cd4*-Cre mice with conditional *tdTomato* reporter mice to follow Cre activity. The fluorescent marker was expressed in 10% of $Lineage^-Sca\text{-}1^+cKit^+$ (LSK) cells (early hematopoietic progenitors) (Figure S1J), allowing *Idh2* and *Tet2* mutations to occur in myeloid-lineage cells. Indeed, myeloid cells from *Idh2* and *Idh2*;*Tet2* animals produced large amounts of D2HG (Figure S1K). Last, no clonal T cell receptor (TCR) β rearrangement was detected in splenic $CD4^+$ T cells from *Idh2*;*Tet2* mice (Figure S1L). Thus, although the *Idh2*;*Tet2* GEMM strain exhibited expansion of Tfh and GC B cell populations, alterations in immature myeloid cells precluded its use for studies of T cell lymphomagenesis.

AT of *Idh2*- and *Tet2*-mutated T cells induces AITL-like disease

To avoid the confounding effects of myeloid disease, we isolated $CD3^+$ cells from 2-month-old WT, *Idh2*, *Tet2*, and *Idh2*;*Tet2* GEMM mice and transplanted them into *TCRa* knockout (KO) recipient mice. This strategy generated 4 AT model strains: t*Idh2*;*Tet2* mice (injected with double-mutant T cells), t*Idh2* and t*Tet2* mice (injected with *Idh2* or *Tet2* single-mutant T cells, respectively), and tWT mice (injected with *Cd4*-Cre T cells). Mice were either injected with PBS (control, P), or sheep red blood cells (SRBC, S) to induce Tfh cell development and generate GC responses[22] (Figure S2A). At the time of transfer, the $CD3^+$ T cell population of all GEMM strains contained the same number of $CD4^+$ cells expressing similar polyclonal TCR repertoires (Figure S2B). Regardless of PBS or SRBC (P/S) treatment, D2HG was detected in $CD3^+$ cells of t*Idh2* and t*Idh2*;*Tet2* mice (Figure S2C).

St*Tet2 and* P/S t*Idh2*;*Tet2* mice showed markedly shorter survival compared with the other AT strains (Figure 1A), with most succumbing to a disease affecting the spleen and lymph nodes (LNs) (Figure 1B). Fluorescence-activated cell sorting (FACS) analysis revealed that, although the overall proportions of $CD3^+$ cells were normal in P/S t*Tet2* and P/S t*Idh2*;*Tet2* mice (Figure S2D), both mutants exhibited a greater proportion of Tfh cells compared with tWT mice (Figure 1C). However, only P/S t*Idh2*;*Tet2* mice showed an increased CD4/CD8 ratio (Figure 1D). St*Idh2*;*Tet2* mice more frequently exhibited elevated $CD4^+CD3^-$ T cells (Figure S2E), a feature of human AITL that likely reflects downregulation of surface TCR expression.[23] Assessment of T cell clonality by FACS and PCR revealed that 30% of P/S t*Idh2*;*Tet2* mice possessed monoclonal T cell populations, and 40% showed oligoclonal populations, with SRBC-treated animals exhibiting monoclonal disease more frequently (Figures 1E and S2F). GC B cells were also elevated in St*Idh2*;*Tet2* mice (Figure 1F). Histological analysis revealed disrupted architecture of the LNs and spleen, arborizing blood vessels, and a cellular infiltrate consisting of $CD3^+CD4^+$ T cells (some with atypical clear cytoplasm), immunoblasts, B cells expressing various levels of B220, and numerous $CD138^+$ plasma

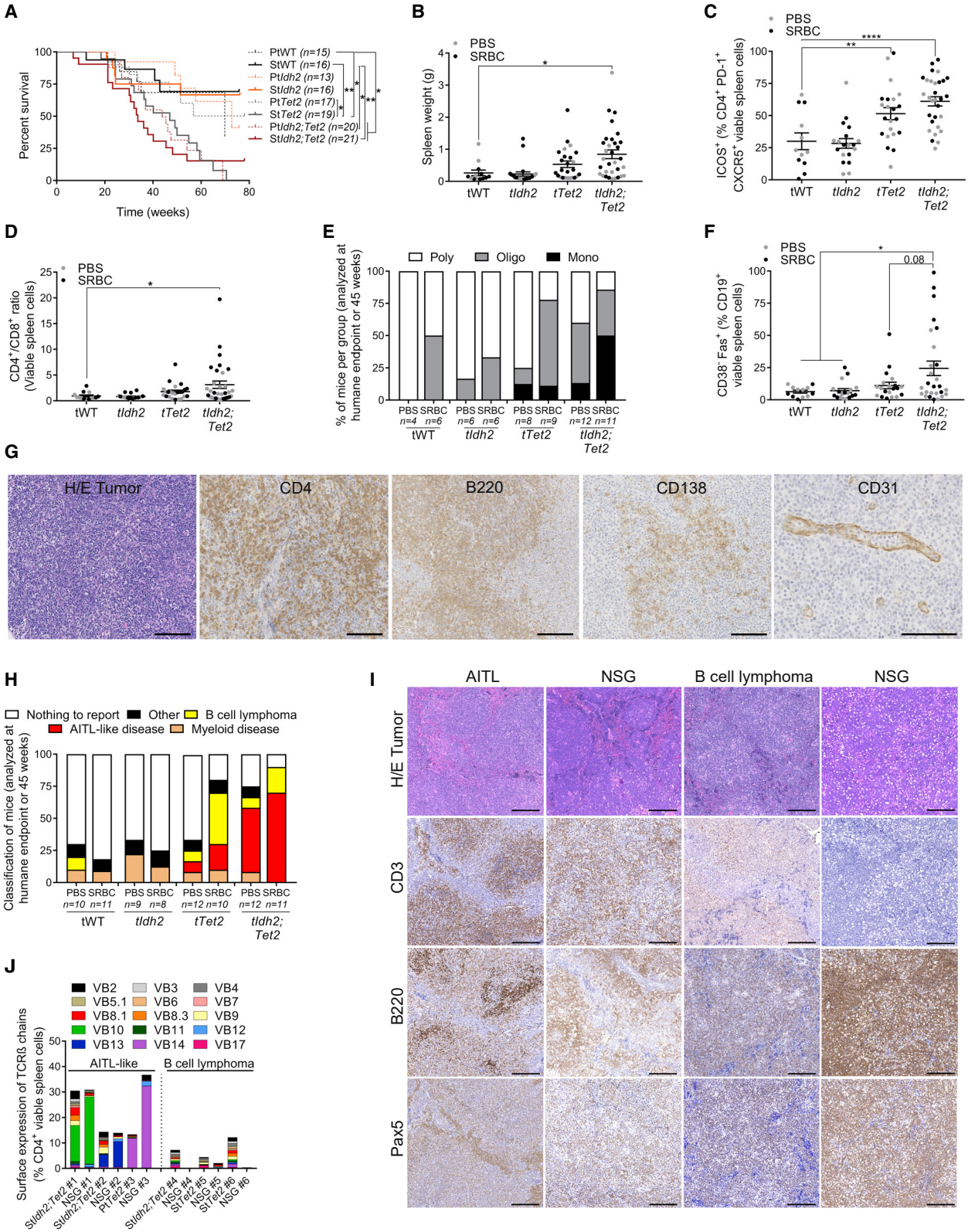

Figure 1. AT of *Idh2*- and *Tet2*-mutated T cells induce AITL-like disease

(A) Kaplan-Meier curves of survival of the indicated AT strains treated with either PBS (P) or SRBC (S).

(B) Spleen weights of the indicated number of AT mice from (A).

(legend continued on next page)

cells (Figure 1G). Thus, St*Idh2*;*Tet2* mice generated PTCL with a Tfh-like phenotype, closely mimicking human AITL.

Interestingly, SRBC treatment had a strong effect on the phenotype of t*Tet2* mice. Like St*Idh2*;*Tet2* mice, St*Tet2* mice experienced weight loss (Figure S2G) and shortened survival (Figure 1A). In addition, 66% of St*Tet2* mice displayed oligoclonal T cell expansion (Figure 1E), and 20% developed an AITL-like disease (Figure 1H), as determined by histologic and immunostaining analyses. However, 40% of St*Tet2* mice died from $CD19^+$ B cell lymphoma (Figure S2H).

To confirm the nature of the T and B lymphomas developing in P/S t*Tet2* and P/S t*Idh2*;*Tet2* mice, we transferred cells from these tumors into non-obese diabetic (NOD)-severe combined immunodeficiency (SCID) gamma (NSG) recipient mice. We found that ~35% of AITL-like malignancies were transplantable: 4 of 10 from P/S t*Idh2*;*Tet2* mice and 1 of 3 from P/S t*Tet2* mice. In each case, a dramatic increase in the CD4/CD8 ratio was observed as well as in the percentages of the Tfh and GC B cell populations (Figures 1I and S2I–S2K). Furthermore, we detected expansion of a monoclonal T cell population that likely represented neoplastic T cells (Figure 1J). With respect to B cell lymphomas, all transplant recipients (2 of 2 from P/S t*Idh2*;*Tet2*, 2 of 2 from St*Tet2*) recapitulated the original disease. B cells with strong expression of B cell markers and the same variable-diversity-joining (VDJ) clonal rearrangement were observed, as well as numerous macrophages imparting a "starry sky" pattern to the tumor (Figures 1I, S2K, and S2L).

In almost all of our AT strains, ~15% of the animals developed a myeloid malignancy with high cKit expression (Figures 1H and S2M). Interestingly, even non-transplanted *TCRa* KO mice developed myeloid disease, suggesting that this pathology arose from endogenous recipient cells rather than from the transferred cells. However, when AT mice developed a lymphoma, cKit levels remained low, minimizing the risk of a concurrent myeloid malignancy. Notably, no T cell lymphomas developed in P/S t*Idh2* or P/S tWT mice (Figure 1H). We concluded that the 60% of St*Idh2*;*Tet2* mice that developed a lethal AITL-like disease were suitable for mechanistic studies.

Altered B cell compartment in AITL-bearing mice

Tfh cells are essential for GC formation and selection of B cells destined to become plasma cells.[24] The overall proportions of splenic $CD19^+$ cells were equivalent in all AT strains (Figure S3A), but naive B cells were decreased in P/S t*Tet2* mice and even more so in P/S t*Idh2*;*Tet2* mice compared with P/S tWT animals (Figure S3B). Detailed FACS and immunohistochemistry (IHC) analyses revealed increased plasma cells in P/S t*Idh2*;*Tet2* mice (Figures 2A and 2B), in line with their increased GC B cells (Figure 1F) and serum immunoglobulin levels (Figure 2C). P/S t*Tet2* animals and, to a lesser extent, P/S t*Idh2*;*Tet2* mice showed an increase in memory B cells compared with P/S tWT controls (Figure S3C). PCR analysis revealed clonal expansion of a B cell population in P/S t*Tet2* and P/S t*Idh2*;*Tet2* mice (Figures 2D and S3D), consistent with their abnormal B cell lymphoproliferation.

Because SRBC treatment appeared to enhance the GC reaction and B cell differentiation in t*Tet2* and t*Idh2*;*Tet2* mice (Figures 1F and 2A), we surmised that the increased neoplastic Tfh cells in these mutants had a profound impact on surrounding normal B cells. During T-dependent immune responses, interactions between normal Tfh cells and B cells generate multiple costimulatory signals, including ICOS/ICOS-L, PD-1/PDL-1, CD40L/CD40, and CD28/CD86.[24] In P/S t*Tet2* and P/S t*Idh2*;*Tet2* Tfh cells, ICOS and PD-1 were increased and CD40L was decreased compared with P/S tWT cells (Figure 2E, left). Although P/S t*Tet2* and P/S t*Idh2*;*Tet2* B cells showed no change in ICOS-L or PDL1 expression, they did exhibit increased CD40 and CD86 (Figure 2E, right). CD40 in B cells promotes their survival and proliferation, GC formation, and memory B cell development,[5] whereas CD86 is a marker of activated B cells that is increased on plasmablasts and memory B cells.[25] These observations suggest that *Tet2* mutation in Tfh cells causes nearby normal B cells to alter their expression of receptors important for Tfh-B cell cross-talk. Concomitantly, these changes can drive clonal B cell proliferation that sometimes results in an aggressive B cell lymphoma in St*Tet2* mice. When Tfh cells bear combined *Tet2* and *Idh2* mutations, GC B cells and plasma cells increase, correlating with the emergence of AITL-like disease associated with a strong, and sometimes clonal, expansion of B cells or plasma cells.

Combined *Idh2* and *Tet2* mutations have no impact on Tfh cell proliferation but alter their phenotype and function

To understand how *Idh2* and *Tet2* mutations modulate T cell behavior, we isolated $CD4^+$ T cells from our GEMM strains and measured their responses to TCR stimulation *in vitro*. *Tet2*-mutated cells showed increased proliferation compared with WT cells, whereas the proliferation of *Idh2* cells was reduced, and that of *Idh2*;*Tet2* cells was unchanged (Figure 3A). We confirmed this proliferative advantage conferred by *Tet2* loss *in vivo* by comparing the proportions of Ki67-positive $CD4^+$ and Tfh cells in our AT strains (Figures S4A and S4B).

We next examined the effects of *Idh2* and *Tet2* mutations on *in vitro* activation of GEMM-derived T cells. Although all strains

(C) FACS quantification of ICOS expression by splenic $CD4^+PD\text{-}1^+CXCR5^+$ cells of AT mice.
(D) Ratio of $CD4^+/CD8^+$ splenic T cells of AT mice.
(E) Percentage of AT mice showing the indicated TCR Vβ clonalities. Poly, polyclonal; Oligo, oligoclonal; Mono, monoclonal.
(F) FACS quantification of splenic $CD19^+CD38^-Fas^+$ cells of AT mice.
(G) Images of an AITL-like tumor (LN) from an St*Idh2*;*Tet2* mouse. H&E staining and IHC to detect CD4, B220, CD138, and CD31 are shown. Scale bars, 100 μm.
(H) Percentages of AT mice that developed the indicated diseases.
(I) Images of an AITL-like tumor from St*Idh2*;*Tet2* mice (column 1), of a B cell lymphoma from St*Tet2* mice (column 3), and the same tissues after transplantation into NSG mice (columns 2 and 4, respectively). H&E staining and IHC to detect CD3, B220, and Pax5 are shown. Scale bars, 250 μm.
(J) Percentage of splenic $CD4^+$ T cells that were isolated from either AITL-like tumors or B cell lymphomas of AT mice and showed surface expression of the indicated TCR Vβ chains as well as TCR Vβ chain expression by $CD4^+$ T cells from the same tissues after transplantation into NSG mice.
The mean ± SEM is shown. *$p < 0.05$, **$p < 0.01$, ***$p < 0.005$, and ****$p < 0.001$, assessed by repeated-measures ANOVA with Tukey multiple-comparisons tests. All images are representative of at least 3 mice/group. See also Figure S2.

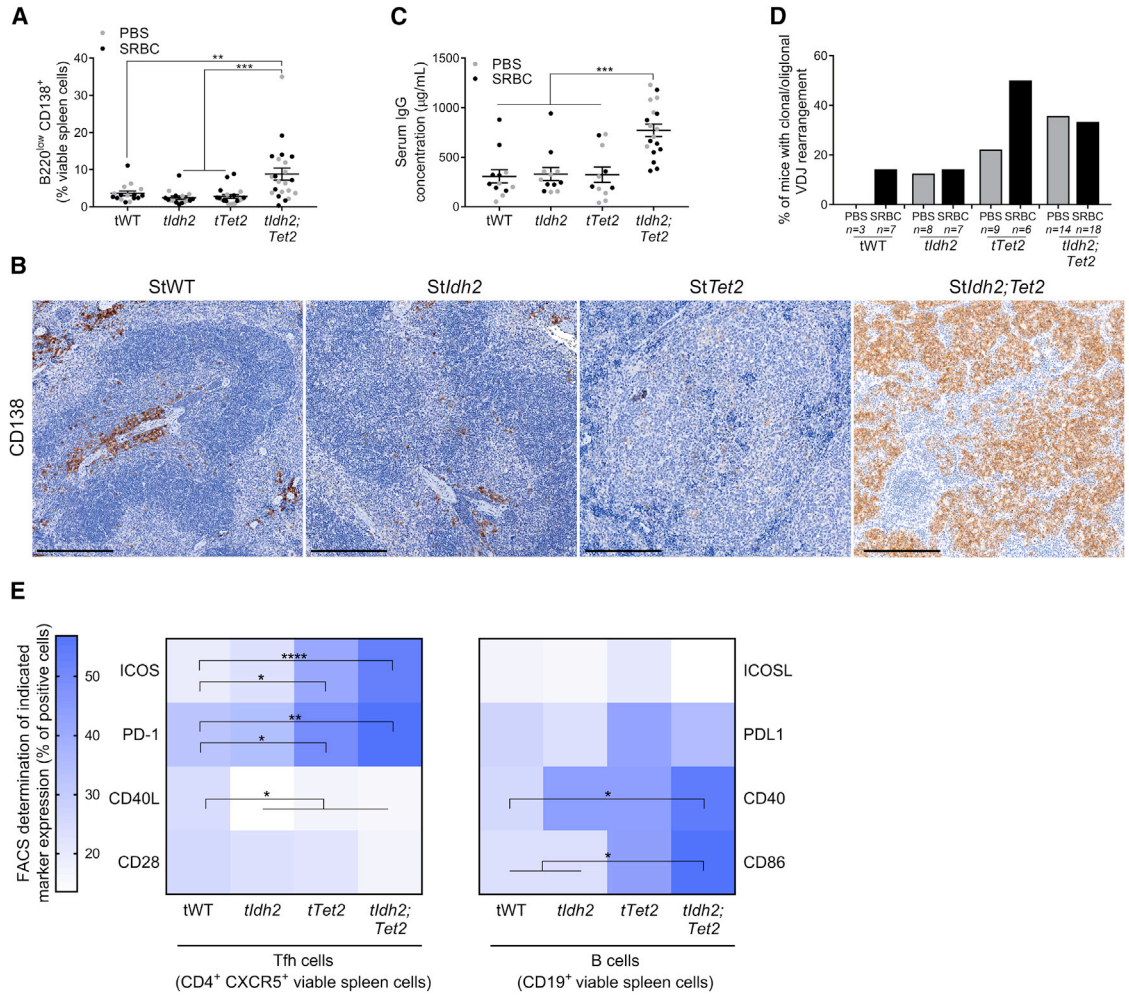

Figure 2. Altered B cell compartment in AITL-bearing mice

(A) FACS quantification of splenic B220^{low}CD138^{+} cells of AT mice.

(B) Images of IHC staining to detect CD138 in spleens of AT mice treated with SRBC (n = 5/group). Scale bars, 250 µm.

(C) Quantification of immunoglobulin G (IgG) levels (µg/mL) in serum of AT mice as determined by ELISA.

(D) Percentages of AT mice showing VDJ rearrangement as determined by PCR analysis of DNA extracted from spleens.

(E) FACS quantification of levels of ICOS, PD-1, CD40L, and CD28 on CD4^{+}CXCR5^{+} splenic Tfh cells and of ICOSL, PDL1, CD40, and CD86 on CD19^{+} splenic B cells isolated from AT mice. tWT (n = 12), *tIdh2* (n = 8), *tTet2* (n = 11), and *tIdh2*;*Tet2* (n = 11) mice.

The mean ± SEM is shown. *p < 0.05, **p < 0.01, ***p < 0.005 and ****p < 0.001, assessed by repeated-measures ANOVA with Tukey multiple-comparisons tests. See also Figure S3.

had equivalent percentages of CD4^{+} T cells, the CD4 mean fluorescence intensity (MFI) was decreased in *Idh2* and *Idh2*;*Tet2* T cells (Figures S4C and S4D), suggesting reduced TCR-mediated signaling. We therefore isolated naive CD4^{+} T cells from each GEMM strain and used an optimized medium to induce mouse Tfh cell differentiation *in vitro*. Compared with their WT counterparts, cultured *Idh2* Tfh cells showed increased ICOS and PD-1 but decreased CD4, with even more pronounced differences in cultured *Idh2*;*Tet2* Tfh cells (Figures 3B–3D). However, CXCR5 was not induced under these conditions (Figure S4E), highlighting the limitations of this approach and the difficulty of replicating complete Tfh cell differentiation *in vitro*.

We next investigated TCR signal transduction in CD4^{+} T cells from each GEMM strain. Following CD3 engagement, we observed a delay or decrease in early phosphorylation events in *Idh2* and *Idh2*;*Tet2* T cells that affected Src family kinases such as Lck, Zap70, and PLCγ1 (Figure S4F). Increased Jnk phosphorylation and decreased Erk phosphorylation also occurred in activated *Idh2* and *Idh2*;*Tet2* T cells, alterations that are known to promote Tfh cell differentiation.[26,27] No differences from the WT were observed in Akt or nuclear factor κB (NF-κB) p65 phosphorylation, but *Tet2* T cells showed a marked increase in p38 phosphorylation (Figure S4F), in line with their increased proliferation capacity.

To explore Tfh cell function, we isolated Tfh cells from our GEMM strains and co-cultured them with WT CD19^{+} B cells (Figure S4G). Almost all CD4^{+} cells recovered from these co-cultures retained their expression of Tfh markers regardless of genotype (Figure S4H). As before, co-cultured *Tet2* T cells displayed increased proliferation and viability compared with WT cells

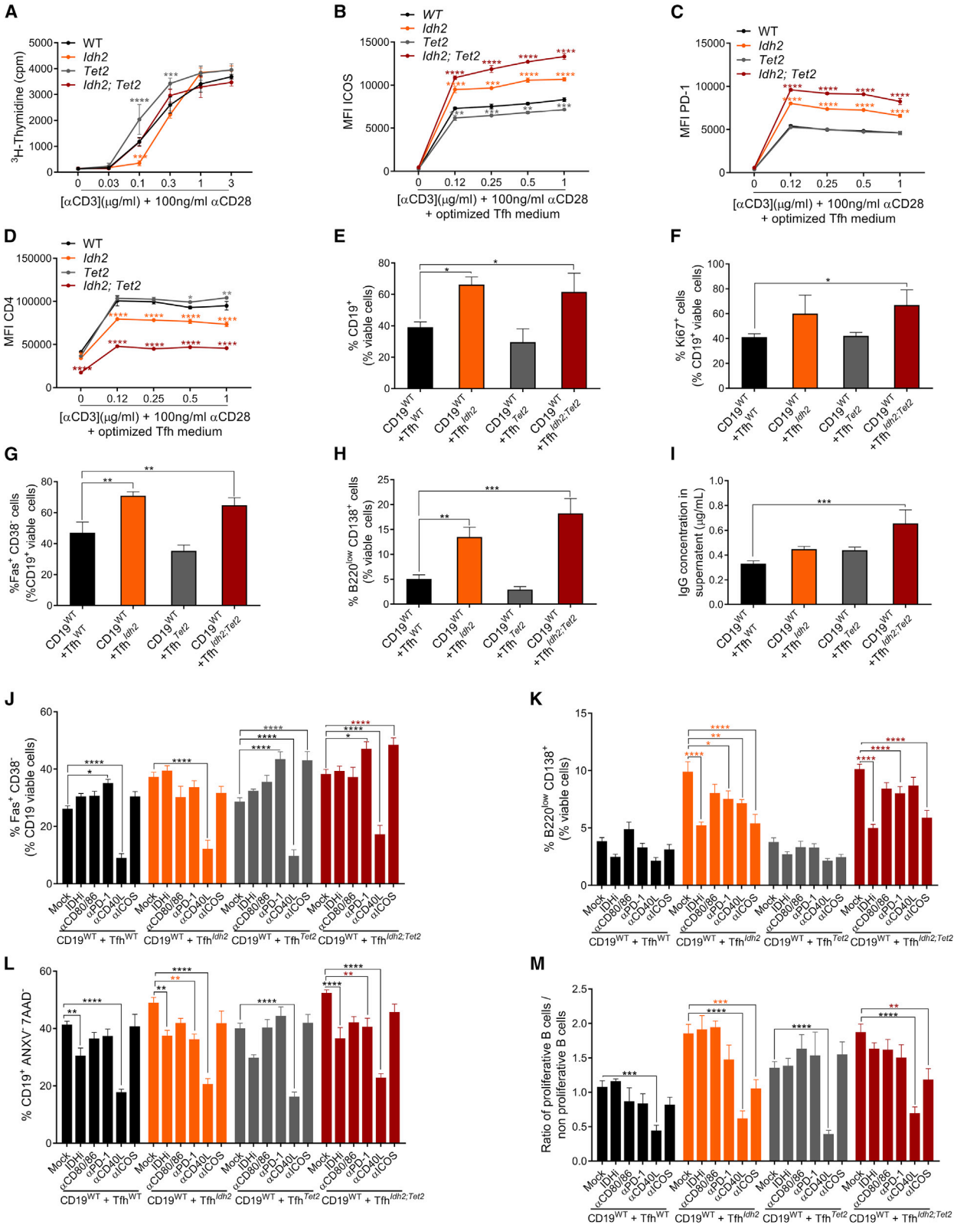

Figure 3. Combined *Idh2* and *Tet2* mutations have no impact on Tfh cell proliferation but alter their phenotype and function

(A) Quantification of [^{3}H]-thymidine incorporation by CD4$^+$ T cells isolated from the indicated strains of GEMM mice and cultured with the indicated concentrations of anti-CD3 plus anti-CD28 antibodies.

(legend continued on next page)

(Figures S4I–S4K). However, in the *Idh2* and *Idh2*;*Tet2* co-cultures, we observed enhanced survival and proliferation of $CD19^+$ cells as well as increases in GC B cell and plasma cell markers (Figures 3E–3H). In addition, the medium of *Idh2*;*Tet2* co-cultures contained enhanced immunoglobulin levels (Figure 3I). These data further suggest that the *Idh2* mutation alters interactions between Tfh and B cells.

We next examined the effects of impairing Tfh-B cell cross-talk in the presence of *Idh2* and/or *Tet2* mutations (Figures 3J–3M). Blockade of CD40 signaling reduced GC B cell differentiation as well as B cell survival and proliferation in all co-cultures (Figure 3J, 3L, and 3M). In contrast, blockade of PD-1 or ICOS in *Tet2* or *Idh2*;*Tet2* co-cultures increased GC B cell differentiation (Figure 3J), suggesting the existence of some negative control mechanisms under these conditions.[28] However, PD-1 and ICOS were critical for plasma cell differentiation in *Idh2* and *Idh2*;*Tet2* co-cultures, with use of an IDH inhibitor reversing the *Idh2* mutation's effect (Figure 3K). PD-1 was also important for B cell survival in *Idh2* and *Idh2*;*Tet2* co-cultures, whereas ICOS supported B cell proliferation (Figures 3L and 3M).

Collectively, these data indicate that *Tet2* inactivation increases T cell proliferation but has no effect on co-cultured normal B cells. In contrast, in the *Idh2*;*Tet2* context, *Idh2* mutation in Tfh cells appears to drive the majority of the effects on B cells. It is important to note that no D2HG was found in B cells co-cultured with *Idh2*-mutated T cells (Figure S4L), indicating that, at least under these specific *in vitro* experimental conditions, D2HG did not directly impair B cell behavior. Thus, mutant *Idh2* leads to enhancements in Tfh cell phenotype and function despite a decrease in TCR signaling.

Combined *Idh2* and *Tet2* mutations affect the transcriptomic and cytokine profiles of Tfh cells

To better understand how *Idh2 and Tet2* mutations affect Tfh cell function, we performed RNA sequencing (RNA-seq) of Tfh cells isolated from our GEMM strains. *Idh2* and *Tet2* Tfh cells showed few transcriptional changes from their WT counterparts, with almost no overlap (Figures 4A, S5A, and S5B). In contrast to the single mutants, *Idh2*;*Tet2* Tfh cells exhibited a unique gene expression pattern with numerous significant changes from the WT and a predominance of downregulated genes (Figures 4A and S5C). Notably, *Cd4* and *Cd247* mRNAs were downregulated in *Idh2*;*Tet2* Tfh cells (Figure S5C), in line with their altered TCR signaling.

Gene set enrichment analysis (GSEA) comparing *Tet2* to WT Tfh cells showed enrichment in genes involved in cell cycling and proliferation and extracellular matrix/metastasis in the mutant cells (Figures 4B and S5B; Table S1), in line with their growth advantage (Figure 3A). Altered expression of genes involved in lipid, leucine, and glutamine metabolism as well as the TCA cycle also occurred in *Tet2* Tfh cells (Figure 4B; Table S1). In contrast, *Idh2*;*Tet2* Tfh cells exhibited enrichment in genes associated with immune responses, chemotaxis, and metastasis (Figure 4B; Table S1). Notably, *Idh2* Tfh cells showed only limited transcriptional changes, with few genes that were differentially expressed related to the immune system or apoptosis (Figure S5A). Because *IDH2* mutation in human AITL almost always co-occurs with *TET2* mutation, we compared GSEA data between our *Idh2*;*Tet2* and *Tet2* Tfh cells and observed enrichment in the double mutant of gene sets related to immune responses and plasma cells as well as a signature found in human AITL tissues (Figure 4B; Table S1).

When we examined genes encoding Tfh cell markers (Figure S5D; Table S2), we observed that *Idh2*;*Tet2* Tfh cells showed decreased expression of *Gpr183/Ebi2*, a chemoattractant receptor that regulates the positioning of normal Tfh cells at the interface of the B cell follicle and the T cell zone,[29] as well as a reduction in *Cd5*, a marker frequently lost or decreased on AITL neoplastic Tfh cells.[30] *Bcl6* was also downregulated in *Idh2*;*Tet2* Tfh cells, but *Klf2* and *Il7r* were upregulated. These findings correlate with a previous study showing that, among normal Tfh cell populations, some cells gradually downmodulate *Bcl6* and upregulate *Il7r* and *Klf2*, giving them a more quiescent phenotype.[31] This $Bcl6^{low}$ Tfh population still resides in GCs and supports B cell responses but migrates more easily from LNs into the circulation.[31] These findings may account for the heavy infiltration of T cells into the lungs, liver, and BM of aged P/S t*Idh2*;*Tet2* mice (Figures S5E and S5F).

To identify expression changes that might impinge on the TME, we examined genes encoding cytokines, receptors, and other molecules important in immune system pathways. Chemokines involved in GC reactions and B cell development, including *interleukin-22* (*IL-22*),[32] *Ccl20*[33] and *IL-4*,[34] were increased in *Idh2*;*Tet2* Tfh cells (Figure 4C and Table S3). Expression levels of numerous genes linked to angiogenesis were also increased, including *Cxcl3*,[35] *Il-22*,[36] *Ccl20*,[37] *Xcl1*, and *Cysltr1*[38] (Figure 4C and Table S3).

These results suggest that *Idh2* and *Tet2* mutations can synergize to reprogram the gene expression and cytokine profiles of Tfh cells. These changes likely modulate the functions of Tfh cells and their interactions with elements of the TME, particularly B cells.

Combined *Idh2* and *Tet2* mutations induce epigenetic modifications of gene promoters that are associated with transcriptomic alterations

Given the anticipated effects of *Idh2* and *Tet2* mutations on epigenetics, we evaluated whether the gene expression changes

(B–D) Mean fluorescence intensity (MFI) values for ICOS (B), PD-1 (C), and CD4 (D) as determined by FACS analysis of naive $CD4^+$ T cells from GEMM mice cultured under conditions optimized to induce Tfh cell differentiation *in vitro*.
(E–H) FACS quantification of viable $CD19^+$ (E), $CD19^+Ki67^+$ (F), $CD19^+Fas^+CD38^-$ (G), and $B220^{low}CD138^+$ (H) cells in co-cultures of WT $CD19^+$ B cells plus Tfh cells from the indicated GEMM strains.
(I) Quantification of IgG levels in supernatants of the co-cultures in (E)–(H) as measured by ELISA.
(J–M) FACS quantification of $CD19^+Fas^+CD38^-$ (J), $B220^{low}CD138^+$ (K), and $CD19^+$ $ANXV^-$ $7AAD^-$ (L) cells and the ratio of proliferative B cells to non-proliferative B cells (M) in the indicated co-cultures after the indicated blocking antibody (α) treatment.
GEMM mice were 2–3 months old; n = 3/group. Mean ± SEM is shown. *$p < 0.05$, **$p < 0.01$, ***$p < 0.005$ and ****$p < 0.001$, assessed by repeated-measures ANOVA with Tukey multiple-comparisons tests. See also Figure S4.

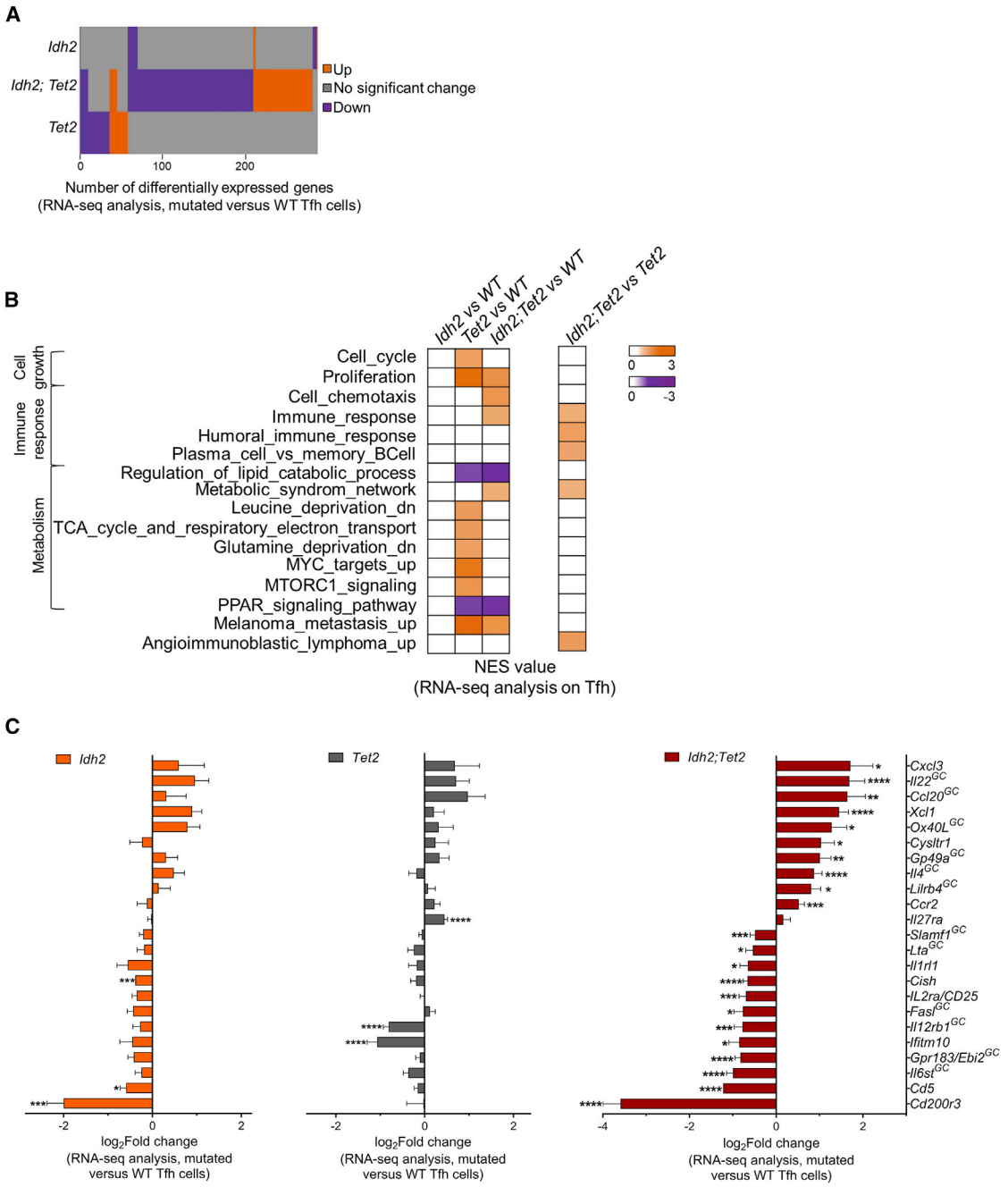

Figure 4. Combined *Idh2* and *Tet2* mutations affect the transcriptomic and cytokine profiles of Tfh cells

(A) Plot depicting the number of differentially expressed genes that were significantly upregulated or downregulated in Tfh cells from GEMM strains as determined by RNA-seq. Log_2 fold change > 0.58, q < 0.01.

(B) GSEA scores for the indicated gene signatures identified in Tfh cells from the indicated GEMM strains versus the WT (left). A comparison of *Idh2*;*Tet2* versus *Tet2* Tfh cells is also shown (right). NES, normalized enrichment score; q < 0.05.

(C) Quantification of the differential expression (log_2 fold change, DESeq2) of the indicated immune-related genes in Tfh cells of the indicated GEMM strains versus the WT. GC, genes involved in the GC reaction. Mean ± SEM is shown. *p < 0.05, **p < 0.01, ***p < 0.005, ****p < 0.001 assessed by repeated-measures ANOVA with Tukey multiple-comparisons tests.

Tfh cells were isolated from 2- to 3-month-old GEMM mice; n = 4/group. Tfh cells of the indicated genotypes were compared with WT Tfh cells. See also Figure S5 and Tables S1 and S3.

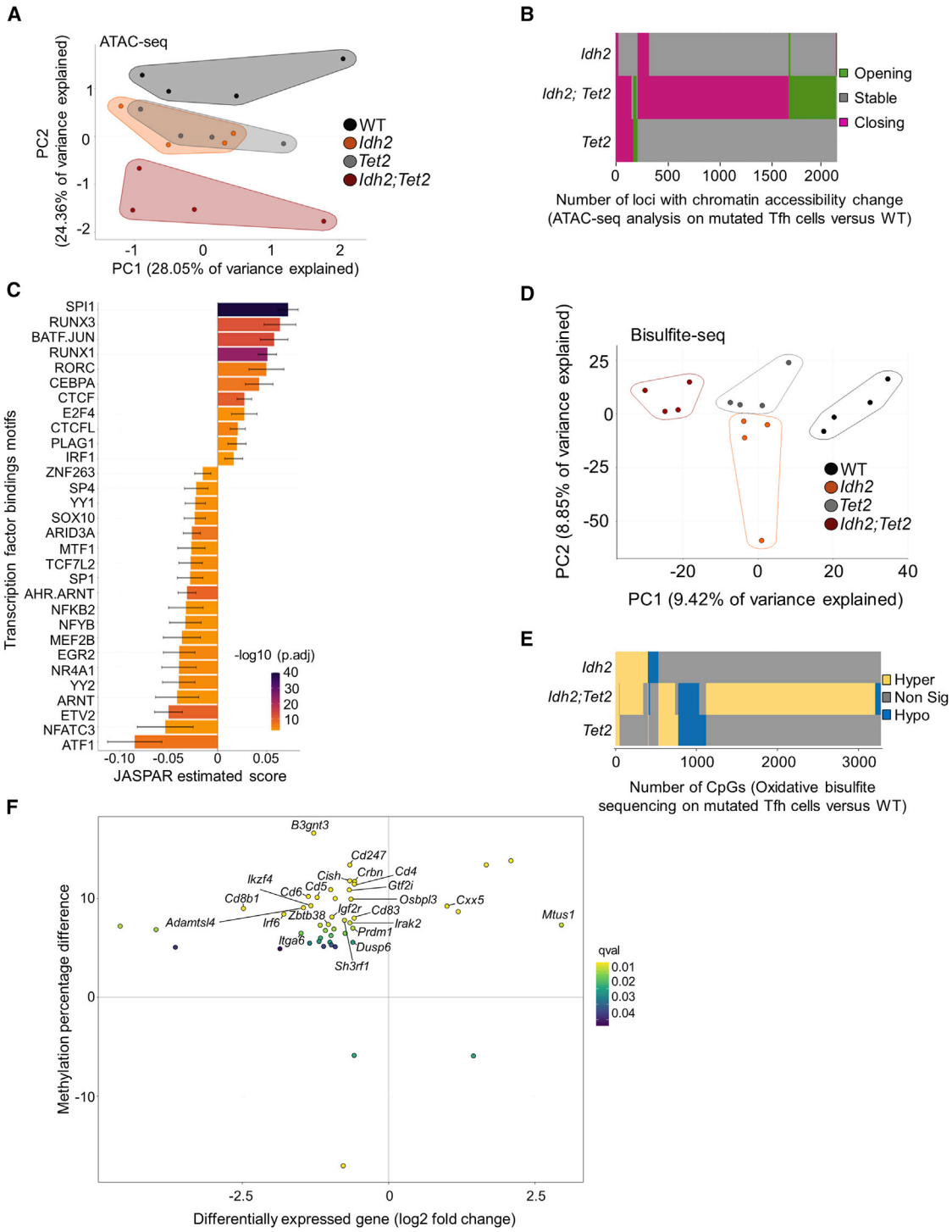

Figure 5. Combined *Idh2* and *Tet2* mutations induce epigenetic modifications of gene promoters that are associated with transcriptomic alterations

(A) PCA based on ATAC-seq of Tfh cells from GEMM strains.

(B) Plot depicting regions of higher (opening) or lower (closing) chromatin accessibility as determined by ATAC-seq of the indicated GEMM strains versus the WT. Log_2 fold change > 0.58, q < 0.01.

(C) Plot of JASPAR analysis of *Idh2*;*Tet2* Tfh cells, presenting the estimated scores for the indicated TF binding motifs at loci gaining (opening) or losing (closing) chromatin accessibility compared with WT Tfh cells. Mean ± SEM is shown.

(D) PCA based on bisulfite sequencing of Tfh cells of the indicated GEMM strains.

(legend continued on next page)

noted above were linked to epigenetic alterations. To examine chromatin accessibility, we conducted assay for transposase-accessible chromatin (ATAC) sequencing on Tfh cells from our GEMM strains. Principal component analysis (PCA) confirmed a clear separation between *Idh2*;*Tet2* Tfh cells and Tfh cells of the other three genotypes (Figure 5A). Comparison of *Idh2*;*Tet2* and WT Tfh cells revealed numerous differentially accessible regions, which were predominantly closing (Figure 5B) and mainly located in introns or gene promoters (Figure S6A).

GSEA revealed that the promoters of genes nearest to differentially accessible regions in *Idh2*;*Tet2* Tfh cells were associated with chemokines, inflammatory responses, transcription factors (TFs; such as Runt-related transcription factor [RUNX], Myc, and Foxp3), TCR signaling, and angiogenesis (Table S4). Chromatin accessibility changes at specific promoters correlated with altered gene expression (Figure S6B; Table S5). Next, we probed the differentially accessible chromatin regions in *Idh2*;*Tet2* Tfh cells for known TF DNA recognition sites. This analysis revealed an enrichment of RUNX1, RUNX3, RAR related orphan receptor C (RORC), and basic leucine zipper transcription factor, ATF-like (BATF)-Jun family motifs in open chromatin areas in *Idh2*;*Tet2* Tfh cells compared with WT Tfh cells (Figure 5C, right). These changes are likely to underlie the altered transcriptional control of key cytokine-encoding genes in the double mutants because *Ccl20* can be regulated by RUNX3,[39] *IL-22* by RORC and RUNX1,[40] and *IL-4* by BATF.[41] In contrast, NF-κB, nuclear factor of activated T cell (NFAT), SP1, and early growth response factor (EGR) DNA recognition sites were enriched in areas of closed chromatin in *Idh2*;*Tet2* Tfh cells (Figure 5C, left).

Because chromatin structure can be modulated by DNA methylation,[42] we performed bisulfite sequencing on Tfh cell DNA from our GEMM strains. PCA indicated that *Idh2*;*Tet2* Tfh cells clustered away from the others (Figure 5D) and presented a hypermethylation profile that minimally overlapped with the single mutants (Figure 5E). The *Idh2*;*Tet2*-specific hypermethylation phenotype was observed across gene promoters, exons, introns, intergenic regions, and CpG islands (Figures S6C and S6D) and was associated with a greater global loss of 5-hydroxymethylcytosine (5-hmc) compared with the other genotypes (Figure S6E).

Over the mouse Tfh cell genome, we found that CpG hypermethylation was mainly associated with chromatin closing (Figure S6F). Moreover, when focusing on differentially methylated regions across gene bodies in *Idh2*;*Tet2* Tfh cells, we found a good correlation between DNA hypermethylation and gene downregulation for several genes (Figure 5F). Interestingly, these genes were involved in T cell activation or T cell commitment (*Cd8b1*, *Cd4*, *Cd247*, *Itga6*, *Igf2r*, *Irak2*, *Irf6*, *Ikzf4*, *Cd83*, *Zbtb38*, *Crbn*, *Sh3rf1*, and *Prdm1)*, regulation of TCR signaling (*Cish*, *Cd5*, *Cd6*, *Gtf2i*, and *Dusp6*), or immune cell infiltration or other immune-related processes (*Adamtsl4*, *B3gnt3*, *Osbpl3*, *Cxx5*, and *Mtus1*) (Figure 5F). We therefore concluded that the combination of *Idh2* and *Tet2* mutations leads to DNA hypermethylation modifications that may contribute in small part to gene expression changes influencing Tfh effector potential.

Combined *Idh2* and *Tet2* mutations alter FasL signaling in Tfh cells

Among the gene expression changes seen in the *Idh2*;*Tet2*-mutated Tfh, those affecting *Fas* and *FasL* were likely to affect Tfh function (Figure 6A). FasL-expressing Tfh cells show a gene expression signature enriched for elements of TCR signaling.[43] Transcriptomic analysis of *Idh2*;*Tet2* Tfh cells indicated decreased *FasL* expression, correlating with downregulation of the TCR signaling elements *Cd4* and *Cd247* (Figures 6B and 6C). Pertinently, the Fas/FasL and TCR signaling pathways are linked to activation-induced cell death (AICD). AICD is a form of apoptosis that is induced by repeated TCR stimulation and leads to deletion of autoreactive T cells so that defective AICD may result in autoimmune disease.[44] ATAC sequencing demonstrated enrichment of closed chromatin areas in regulatory elements proximal to genes involved in "cell death by apoptosis" (Table S4). These results correlated with the enrichment of DNA recognition motifs for TFs controlling FasL transcription (Egr2, NF-κB, NFAT, and SP1) within closed chromatin areas in *Idh2*;*Tet2* Tfh cells (Figure 5C). This convergence of data pointing to Fas/FasL alterations prompted us to investigate their status in co-cultures and in our AT strains.

When *Idh2*;*Tet2* Tfh cells were co-cultured with WT B cells, the numbers of $FasL^+$ Tfh cells were decreased compared with co-cultures containing WT T cells (Figure 6D), whereas Fas^+ B cells were increased (Figure 6E). Co-culture with *Idh2* or *Idh2*;*Tet2* Tfh cells increased B cell viability compared with culture with Tfh cells of the other genotypes (Figure 6F). Notably, treatment of co-cultures with a Fas agonist antibody decreased B cell viability in all four cases (Figure 6F).

We confirmed this decrease in $FasL^+$ Tfh cells and increase in Fas^+ B cells in P/S t*Idh2*;*Tet2* mice (Figures 6G and 6H). We isolated total spleen cells from all four AT strains and treated them (or not) *in vitro* with recombinant human FasL protein. GC B cells from P/S t*Idh2*;*Tet2* mice showed increased apoptosis and decreased viability in response to FasL compared with untreated cells (Figures 6I and 6J), whereas GC B cells of the other three genotypes showed no such changes. Thus, the presence of *Idh2*;*Tet2* Tfh cells not only increases the proliferation and differentiation of B cells but also bolsters their survival by downregulating Fas-mediated apoptosis.

The effects of *Idh2* mutation on the TME of St*Idh2*;*Tet2* tumors share similarities with those found in *IDH2*-mutated AITL patients

To compare the effects of *Idh2*;*Tet2* double mutation on Tfh cells with those seen in AITL-like tumors, we performed RNA-seq of LNs or tumors isolated from our SRBC-treated AT strains. Tumors from St*Idh2*;*Tet2* mice displayed a profoundly altered transcriptome compared with LNs of the other three genotypes (Figure S7A). Among upregulated genes, we identified Tfh

(E) Plot depicting significantly hyper- or hypomethylated CpG residues as determined by bisulfite sequencing analysis of the indicated GEMM strains versus the WT. Non Sig, no significant change.
(F) Plot depicting the correlation between differential methylation and change in gene expression for *Idh2*;*Tet2* Tfh cells compared with WT Tfh cells.
Tfh cells were isolated from 2- to 3-month-old GEMM mice; n = 4/group. See also Figure S6 and Table S4.

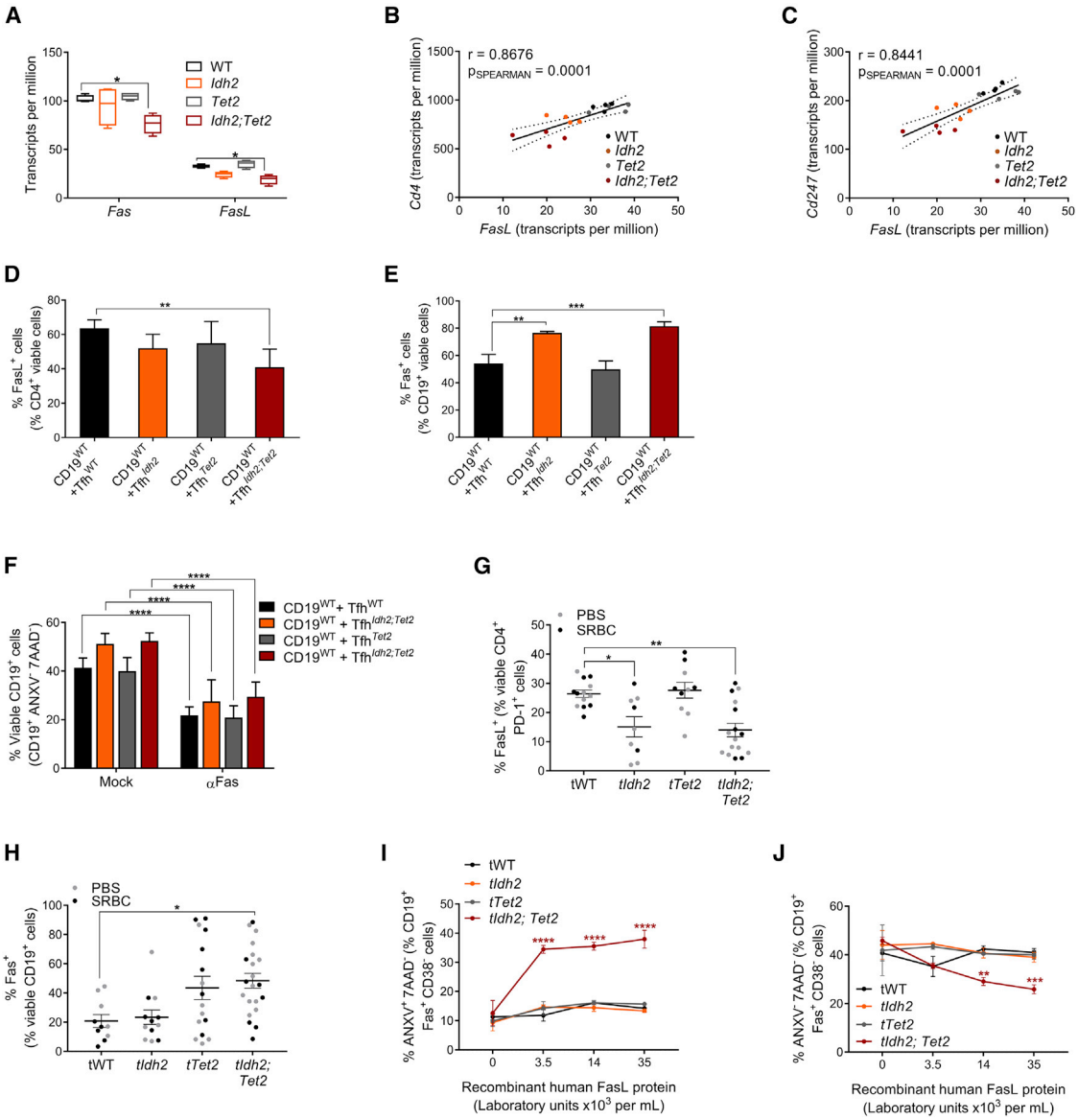

Figure 6. Combined *Idh2* and *Tet2* mutations alter FasL signaling in Tfh cells

(A) Quantification of *Fas* and *FasL* transcripts in Tfh cells of GEMM strains as determined by RNA-seq.

(B and C) Plots of correlations between *FasL* and *Cd4* mRNAs (B) and *FasL* and *Cd247* mRNAs (C), based on RNA-seq of Tfh cells from GEMM strains.

(D–F) FACS quantification of viable $CD4^+FasL^+$ (D), $CD19^+Fas^+$ (E), and $CD19^+ANXV^-7AAD^-$ (F) cells in co-cultures of WT $CD19^+$ B cells plus splenic Tfh cells from GEMM strains (n = 3).

(G and H) FACS quantification of viable $CD4^+PD\text{-}1^+FasL^+$ (G) and $CD19^+Fas^+$(H) splenic cells from AT strains.

(I and J) FACS quantification of $CD19^+$ Fas^+ $CD38^-$ $ANXV^+7AAD^-$ (I) and $CD19^+$ Fas^+ $CD38^-$ $ANXV^-7AAD^-$ (J) splenic cells that were isolated from AT strains and treated *in vitro* with the indicated number of laboratory units of recombinant FasL protein (n = 3).

(A–C) Tfh cells were isolated from 2- to 3-month-old GEMM mice; n = 4/group.

(D–J) The mean ± SEM is shown.

*p < 0.05, **p < 0.01, ***p < 0.005, ****p < 0.001 assessed by repeated-measures ANOVA with Tukey multiple-comparisons tests.

markers (*Il-21*, *Tox*, and *Tnfrsf4)* and genes involved in angiogenesis (*Angptl2*, *Cxcl2*, and *Spp1*). Several B cell-associated genes (*Cd70*, *Gapt*, and *Ighd*) as well as multiple genes linked to the immune system (*Il1r2*, *Il5ra*, and *Ccr8)* were also altered (Figure S7B). We next conducted GSEA of differentially expressed genes in St*Idh2*;*Tet2* AITL-like tumors and found an enrichment of genes involved in the Tfh signature, endothelial cell development, GC B cell functions, metastasis, and plasma cells (Figure S7C). Furthermore, the same gene expression pattern found in *Idh2*;*Tet2* Tfh cells was also preserved in St*Idh2*;*Tet2* tumors (Figure 7A, top).

Interestingly, gene signatures of our St*Idh2*;*Tet2* AITL-like tumors were found to be enriched in two previously published cohorts of human AITL tumors mutated for *IDH2*[21,45] (Figure 7A,

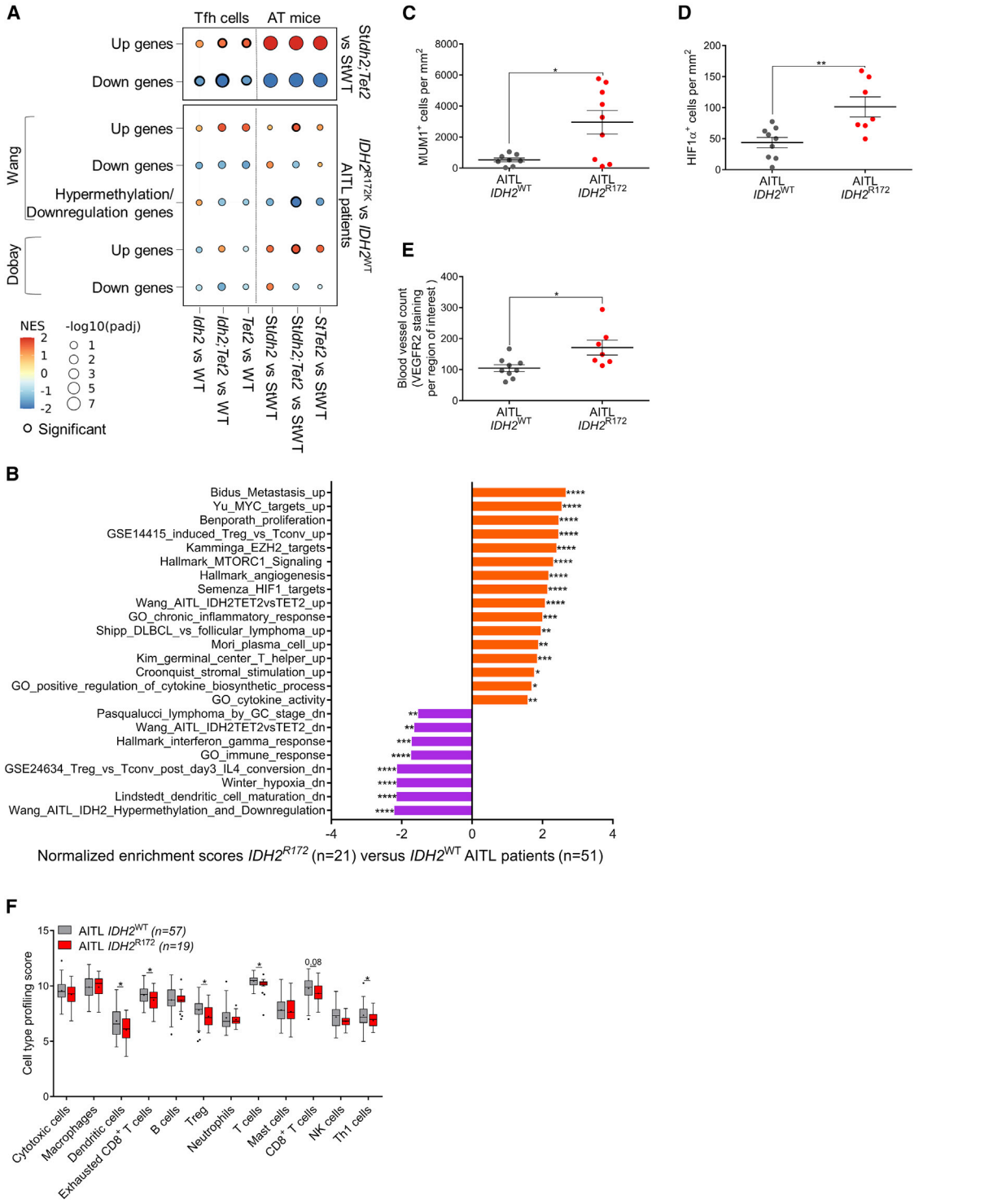

Figure 7. The effects of *Idh2* mutation on the TME of *Stidh2;Tet2* tumors share similarities with those found in *IDH2*-mutated AITL patients

(A) GSEA scores of enrichment for the indicated gene signatures identified in either Tfh cells or SRBC-treated AT mice using the indicated datasets. Normalized enrichment score (NES); $\log_2$ fold change > 0.58, q < 0.01.

(B) NES computed by GSEA of a dataset that was described by Dobay et al.[45] and compared *IDH2*^{R172K} AITL patients (n = 21) with *IDH2*^{WT} AITL patients (n = 51), as analyzed by Affymetrix technology.

(legend continued on next page)

bottom). Moreover, Wang et al.[21] demonstrated that *IDH2*-mutated cases showed upregulation of Tfh-associated genes as well as those predicting activation of the vascular endothelial growth factor pathway. These authors also detected promoter hypermethylation and expression downregulation of several genes involved in TCR signaling and T cell differentiation, reminiscent of our mouse data (Figures 5F, 7A, and S7C).

To determine whether *IDH2* mutation affects the TME in human AITL tumors (as we found in our AT mice), we performed GSEA of the Dobay cohort of AITL patients[45] and noted that samples with $IDH2^{R172}$ mutations showed enrichment of genes linked to Tfh cells, angiogenesis, metabolism, hypoxia, metastasis, and plasma cells (Figure 7B). The signature of hypermethylation/downregulation described by Wang et al.[21] was also found to be enriched in tumors of these patients. These data suggest that our St*Idh2*;*Tet2* mouse model recapitulates critical features seen in the tumors and TME of human *IDH2*-mutated AITL.

An important highlight in all of these studies is the emergence of a critical role for *Idh2* in plasma cells and angiogenesis, which are vital elements of the AITL TME. To probe this finding further, we selected a few patients from a new AITL cohort whose mutational status had been determined with greater sensitivity through use of next-generation sequencing. We histologically compared tumor sections from individuals with either $IDH2^{WT}$ or $IDH2^{R172}$-mutant AITL. $IDH2^{R172}$-mutant AITL tumors showed enhanced MUM1 and HIF1α staining as well as elevated numbers of $VEGFR2^{+}$ blood vessels compared with $IDH2^{WT}$ tumors, validating the enriched gene signatures for plasma cells and angiogenesis in the former (Figures 7C–7E). We then applied a specific panel from Nanostring Technology to this same AITL patient cohort to determine the differential expression of genes involved in tumor biology, the TME, and immune responses. This approach revealed that only a few genes were differentially expressed between $IDH2^{WT}$ and $IDH2^{R172}$-mutated AITL tumors, but among these, Tfh-associated genes (*CXCL13* and *LIF*) as well as *VEGFA* were upregulated (Figure S8). Nanostring nCounter cell type profiling revealed that $IDH2^{R172}$-mutated AITL tumors showed decreases in signatures of dendritic cells and regulatory T cells and Th1 and $CD8^{+}$ T cells compared with $IDH2^{WT}$ AITL tumors (Figure 7F). These results indicate that *IDH2* mutation in AITL alters the TME and gene expression patterns related to the immune system in a manner distinct from changes seen in $IDH2^{WT}$ AITL.

DISCUSSION

In this study, we generated and analyzed two mouse models to elucidate how $IDH2^{R172}$ mutation contributes to AITL pathogenesis. Our observations suggest that a major consequence of *Idh2* mutation in *Tet2*-deleted Tfh cells is modification of the cross-talk that occurs between neoplastic Tfh cells and other nearby normal cell types; these alterations then lead to establishment of the prototypical AITL TME (Figure 8, left). Our observations provide a plausible roadmap toward understanding the etiology of lymphomagenesis in *IDH2*-mutated AITL and a heretofore elusive mouse model to study *Idh2* mutation in this disease.

Unlike other nodal Tfh PTCLs, AITL exhibits a prominent reactive TME with large B cells and arborizing vascularization.[46] Although *TET2*, *RHOA*, and *DNMT3A* mutations are detected at similar frequencies in AITL and nodal Tfh PTCL, *IDH2* mutations are restricted to AITL.[45] By showing that *Idh2* mutations in mouse Tfh cells drive profound alterations in surrounding normal B cells, our study explains the unique relationship between *IDH2* mutation and AITL TME composition. A key finding from our AT model is that normal B/plasma cells undergo clonal expansion in recipient mice transplanted with *Tet2* or *Idh2*;*Tet2* T cells. AITL patients frequently show abnormal B cell proliferation, but these B cells are often positive for Epstein-Barr virus (EBV^{+}) and bear genetic anomalies like *TET2* or *DNMT3A* mutations, suggesting a role of these factors in driving B cell lymphoproliferation.[7,47] However, we have shown in mice that EBV^{-} B cells with normal genomes are driven to clonally expand after interacting with *Tet2* or *Idh2*;*Tet2* T cells. We hypothesize that the mutated Tfh cells deliver an aberrant signal that induces genomic instability and oncogenic alterations in B cells, promoting their clonal expansion, but this possibility requires more investigation.

Another hypothesis could be related to the recent non-autonomous role described for D2HG in the TME and especially the effects of this oncometabolite on $CD8^{+}$ T cells.[48] In our co-culture model, we were not able to detect D2HG in B cells. D2HG is poorly cell penetrative, and, to date, expression of D2HG transporters has been described for renal cells, astrocytes, and T cells but not other cell types.[49] Although it remains possible that D2HG can modulate B cells *in vivo*, it may be relevant to investigate whether D2HG can influence cell types other than T cells in the TME. It should also be noted that B cell lymphoproliferation was observed in t*Tet2* mice only after SRBC stimulation and that no *in vitro* impact on normal B cells occurred during co-culture with *Tet2* Tfh cells (unlike co-culture with *Idh2* or *Idh2*;*Tet2* Tfh cells). Our model may therefore be useful for improving our understanding of normal Tfh/B cell cross-talk and plasma cell differentiation.

Our work has implications for avenues of AITL treatment. The observed increase in B cells could also be due to reduced B cell apoptosis, which would correlate with the decreased FasL displayed by *Idh2*;*Tet2* Tfh cells. Importantly, B cells in our AT model maintained their sensitivity to apoptosis induced by exogenous FasL, a characteristic that could be therapeutically exploited in AITL patients refractory to conventional treatments. Moreover, we showed that targeting the cross-talk between Tfh cells and B cells using anti-PD-1, anti-ICOS, or anti-CD40L antibodies reduced the B cell population, implying that this approach could have an impact on disease progression. Inhibition of ICOS and CD40 signaling has already been performed

(C–E) Quantification of $MUM1^{+}$ cell density (C), $HIF1\alpha^{+}$ cell density (D), and $VEGFR2^{+}$ blood vessels (E) in tumor sections from $IDH2^{R172K}$ AITL patients versus $IDH2^{WT}$ AITL patients as determined by IHC. Values are for individual sections with the mean ± SEM also shown.
(F) Box and whiskers plots showing the cell type profiling scores for tumors of AITL patients that were classified according to *IDH2* mutational status and analyzed by Nanostring nCounter.
*$p < 0.05$, **$p < 0.01$, ***$p < 0.005$ ****$p < 0.001$ assessed by repeated-measures ANOVA with Tukey multiple-comparisons tests. See also Figures S7 and S8.

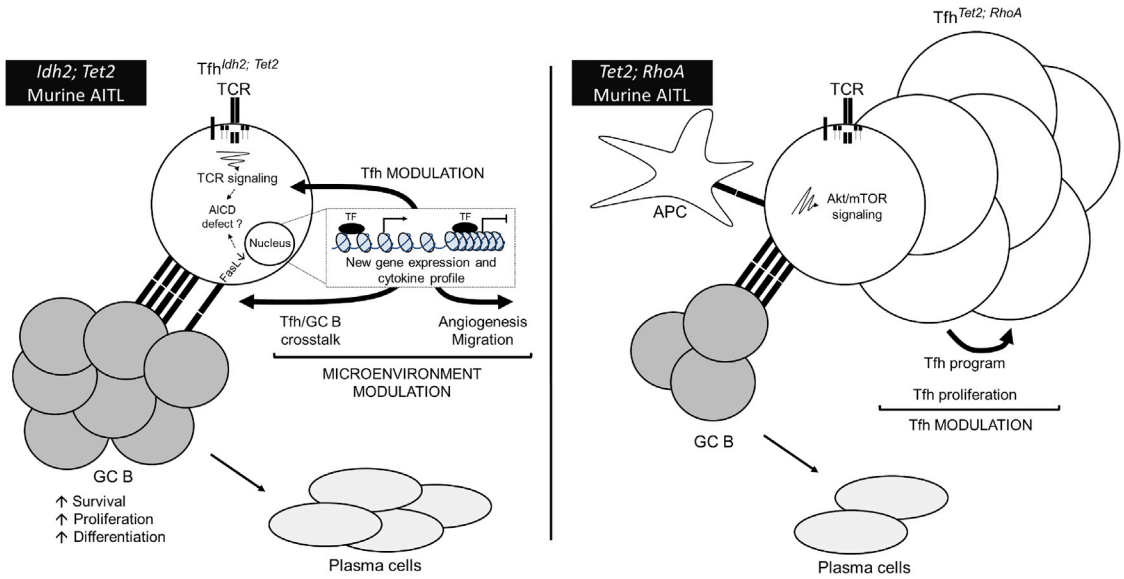

Figure 8. *Idh2* mutation in Tfh cells affects the AITL TME

Graphical summaries illustrating (left) the effects of combined *Idh2* and *Tet2* mutations on Tfh cell function and their impact on the surrounding TME and (right) the effects of combined *Tet2* and *RhoA* mutations on Tfh cells as described in other AITL mouse models.[13–16]

in AITL mouse models featuring *Tet2* and *RhoA* mutations, with encouraging results.[5,20] It will thus be interesting to compare how adding an *Idh2* mutation to *Tet2* and *RhoA* mutations affects responses to these treatments. Use of an IDH inhibitor might also be beneficial if it can correct altered cytokine secretion by neoplastic Tfh cells; such an approach could have broad effects by targeting multiple cell types in the TME.

Finally, DNA demethylating agents may be worthy of trial because several negative regulators of TCR signaling are hypermethylated and downregulated in *IDH2*-mutated AITL patients[21] and in our AT model. Downregulation of TCR-negative regulators could lead to increased signaling through other pathways potentiating inappropriate costimulation of Tfh cells. In theory, DNA demethylating agents such as azacitidine or decitabine could epigenetically reprogram *IDH2*;*TET2*-mutant Tfh cells and reverse their abnormal function. It should be noted, however, that the DNA hypermethylation we detected in our model could be correlated with only a few actual gene expression changes in our mutated Tfh cells. This discrepancy might be due to the technical limitations of this particular experiment. Other types of assays, such as a 5-hmC pull-down experiment, would increase our understanding of the correlation between DNA methylation and gene expression in our model. In addition, given the known effects of *Idh* mutations, other mechanistic alternatives to dysregulation of DNA methylation, such as altered histone methylation, should be explored in future studies.

Our work also sheds light on an intriguing issue in the field: the co-existence of *TET2* and *IDH2* mutations in AITL but the mutual exclusion of these mutations in acute myeloid leukemia (AML). We showed in our GEMM strains that *Idh2* mutation and *Tet2* deletion act synergistically on myeloid cells to drive aggressive myeloid disease. Thus, the *IDH2*^{R172K} mutation, even in AML, has consequences other than *TET2* inhibition. *Idh2*-mutated Tfh cells had a strong impact on normal B cells in co-cultures, but *Idh2* mutation alone had little effect on T cell transcriptomics and epigenetics or on mouse phenotype or survival. In our AT mice, the *Idh2* and *Tet2* mutations had to be combined in Tfh cells before significant numbers of animals developed AITL-like disease, consistent with the dominant co-occurrence of *TET2* and *IDH2* mutations in human AITL. Why *IDH2* mutation drives oncogenesis only in the presence of *TET2* mutation is still not completely defined, but we did show that *Idh2*;*Tet2* T cells produce more D2HG than *Idh2* T cells, potentially resulting in greater inhibition of αKG-dependent dioxygenases. This heightened ability to synthesize D2HG could be related to the altered metabolic gene expression programs in *Tet2* Tfh cells. Furthermore, we showed that *Idh2* mutation alone decreases T cell proliferation and TCR signaling. In this context, *Tet2* mutation may help to maintain the proliferation and survival of *Idh2*-mutated Tfh cells.

We found that the combination of *Idh2* plus *Tet2* mutations downregulated FasL and TCR signaling within Tfh cells. This downregulation should theoretically protect the mutant T cells from the AICD induced by excessive TCR signaling; such AICD controls T cell expansion and must be overridden during oncogenesis. Nevertheless, excessive T cell signaling is often described in AITL patients,[50] which may reflect additional oncogenic mutations such as *RHOA* alterations or other signaling emanating from the TME. Indeed, *Rhoa*^{G17V} mutation combined with *Tet2* loss results in AITL-like disease in various mouse models.[13] *Tet2* loss alters T cell epigenetics, while *RhoA* mutation activates TCR signaling, proliferation, and Tfh differentiation (Figure 8, right). Although our AT models lack a specific TCR-activating mutation, such as RHOA, stimulation of TCR signaling is likely to have occurred during the homeostatic proliferation that follows transplantation and SRBC injection. It would thus be of great interest to generate an *Idh2*/*Tet2*/*RhoA*-mutated mouse model to potentially directly connect epigenetic modifications to TCR signaling alterations in AITL.

In conclusion, AITL is a complex malignancy involving neoplastic Tfh cells and a prominent TME filled with reactive B cells and plasma cells. Our study has revealed the pivotal role of *Idh2* mutation in combining with *Tet2* loss to define the characteristics of the AITL TME. Our work also establishes a sound rationale for therapeutically targeting the cross-talk between neoplastic Tfh cells and the TME as a new strategy for treating AITL patients.

STAR★METHODS

Detailed methods are provided in the online version of this paper and include the following:

- KEY RESOURCES TABLE
- RESOURCE AVAILABILITY
  - Lead contact
  - Materials availability
  - Data and code availability
- EXPERIMENTAL MODEL AND SUBJECT DETAILS
  - Mice
  - Tumor transplantation into NSG mice
  - Human AITL studies
- METHODS DETAILS
  - Mouse cell isolation
  - Adoptive T cell transfer to generate AT strains and GC reaction induction *in vivo*
  - Flow cytometry and antibodies
  - Cell proliferation
  - *In vitro* Tfh cell differentiation
  - Detection of TCR signaling
  - Co-culture of Tfh cells and B cells
  - FasL-induced apoptosis
  - Annexin-7AAD staining
  - Blocking antibodies and IDHi *in vitro* assays
  - Histology and immunohistochemistry
  - Staining intensity
  - T cell clonality
  - B cell clonality
  - IgG levels
  - D2HG levels
  - Immunoblotting
  - Dot blots
  - Preparation of samples for bulk RNA-seq, bisulfite-seq and ATAC-seq
  - Transcriptomic analysis
  - Oxidative reduced representation bisulfite sequencing
  - ATAC-sequencing
  - Nanostring gene expression profiling
  - Gene Set Enrichment Analysis (GSEA)
  - Statistical analyses

SUPPLEMENTAL INFORMATION

Supplemental information can be found online at https://doi.org/10.1016/j.ccell.2023.01.003.

ACKNOWLEDGMENTS

This study was supported by SCOR grant 7013-17 from the Leukemia and Lymphoma Society (to T.W.M., P.G., A.M., and C.E.M.) and by a Canadian Institutes of Health Research Foundation grant (to T.W.M.). J.L. was supported by an Irvington Fellowship from the Cancer Research Institute (USA). F.L. is supported by the Fondation ARC pour la Recherche sur le Cancer (PJA20191209597). We thank Ross Levine, Shigekazu Nagata, David Brooks, Maureen Cox, Robert Nechanitzky, Mathieu Lupien, and Paul Guilhamon for scientific advice and helpful discussions; Irene Ng for administrative assistance; Drew Wakeham, Jennifer Silverster, and Annick You-Ten for technical help in the laboratory; and Mary Saunders for scientific editing of the manuscript. The authors are also grateful to Lily Zhou of the Princess Margaret HistoCore (UHN) for histological imaging; all staff of the Animal Resource Centre at Princess Margaret Hospital for animal care; Eric Xueyu Chen and Zhang Wen-Jiang of the Cancer Clinical Research Unit at Princess Margaret Cancer Centre (PMCC) for D2HG dosage analyses; Kyle Gill and Ryan Harrietha of PMCC for help with genotyping; Arian Khandani, Aleks Spurmanis, and Frances Tong of the PMFlow Cytometry Core Facility (UHN) for identification and isolation of Tfh cell populations; and Alicia Alonso of the Weill Cornell Medicine Epigenomics Core for technical support.

AUTHOR CONTRIBUTIONS

Conceptualization, J.L., F.L., J. Fortin, T.S., A.M., P.G., and T.W.M.; methodology, J.L., F.L., C. Meydan, J. Foox, S.E.G., D.-L.M., G.S.D., C.T., K.H., J.H., L.K.S., A.J.E., D.B., C.E.M., and A.M.; software, C. Meydan, J. Foox, and S.E.G.; formal analysis, J.L., C. Meydan, J. Foox, S.E.G., and D.-L.M.; investigation, J.L.; resources, J.L., F.L., C. Meydan, J. Foox, S.E.G., D.B., T.B., L.d.L., C.E.M., A.M., P.G., and T.W.M.; data curation, J.L., C. Meydan, and J. Foox; writing – original draft, J.L.; writing – review & editing; J.L., F.L., S.E.G., J. Fortin, T.S., L.d.L., A.M., P.G., and T.W.M.; supervision, J.L. and T.W.M.; project administration, T.W.M.; funding acquisition, T.B., C.E.M., A.M., P.G., and T.W.M.

DECLARATION OF INTERESTS

A.M. has consulted for Epizyme, Constellation, Daiichi Sankyo, AstraZeneca, BMS, Janssen, and ExoTherapeutics; has research funding from Epizyme, Janssen, Daiichi Sankyo, and AstraZeneca; and is on the advisory board of KDAC. C.E.M. is a cofounder and board member for Biotia and Onegevity Health as well as an advisor or grantee for Abbvie, ArcBio, Daiichi Sankyo, DNA Genotek, Tempus Labs, and Whole Biome. T.W.M. holds equity in Treadwell Therapeutics Inc. and Agios Pharmaceuticals and is a consultant for AstraZeneca and Tessa Therapeutics.

Received: February 24, 2022
Revised: April 11, 2022
Accepted: January 11, 2023
Published: February 2, 2023

REFERENCES

1. de Leval, L., Parrens, M., Le Bras, F., Jais, J.P., Fataccioli, V., Martin, A., Lamant, L., Delarue, R., Berger, F., Arbion, F., et al. (2015). Angioimmunoblastic T-cell lymphoma is the most common T-cell lymphoma in two distinct French information data sets. Haematologica *100*, e361–e364. https://doi.org/10.3324/haematol.2015.126300.
2. De Leval, L., Rickman, D.S., Thielen, C., Reynies, A.d., Huang, Y.L., Delsol, G., Lamant, L., Leroy, K., Brière, J., Molina, T., et al. (2007). The gene expression profile of nodal peripheral T-cell lymphoma demonstrates a molecular link between angioimmunoblastic T-cell lymphoma (AITL) and follicular helper T (TFH) cells. Blood *109*, 4952–4963. https://doi.org/10.1182/blood-2006-10-055145.
3. Chiba, S., and Sakata-Yanagimoto, M. (2020). Advances in understanding of angioimmunoblastic T-cell lymphoma. Leukemia *34*, 2592–2606. https://doi.org/10.1038/s41375-020-0990-y.
4. Witalis, M., Chang, J., Zhong, M.C., Bouklouch, Y., Panneton, V., Li, J., Buch, T., Kim, S.J., Kim, W.S., Ko, Y.H., et al. (2020). Progression of AITL-like tumors in mice is driven by Tfh signature proteins and T-B cross talk. Blood Adv. *4*, 868–879. https://doi.org/10.1182/bloodadvances.2019001114.

5. Fujisawa, M., Nguyen, T.B., Fukumoto, K., Suma, S., Makishima, K., Kaneko, C., Yen, T., Nguyen, M., Usuki, K., Narita, K., et al. (2022). Clonal germinal center B cells function as a niche for T-cell lymphoma. Blood *140*, 1937–1950. https://doi.org/10.1182/blood.2022015451/1912535/blood.2022015451.pdf.

6. Tan, B.T., Warnke, R.A., and Arber, D.A. (2006). The frequency of B- and T-cell gene rearrangements and Epstein-Barr virus in T-cell lymphomas: a comparison between angioimmunoblastic T-cell lymphoma and peripheral T-cell lymphoma, unspecified with and without associated B-cell proliferations. J. Mol. Diagn. *8*, 466–475. https://doi.org/10.2353/jmoldx.2006.060016.

7. Zettl, A., Lee, S.S., Rüdiger, T., Starostik, P., Marino, M., Kirchner, T., Ott, M., Müller-Hermelink, H.K., and Ott, G. (2002). Epstein-Barr virus-associated B-cell lymphoproliferative disorders in angloimmunoblastic T-cell lymphoma and peripheral T-cell lymphoma, unspecified. Am. J. Clin. Pathol. *117*, 368–379. https://doi.org/10.1309/6UTX-GVC0-12ND-JJEU.

8. Lemonnier, F., Couronné, L., Parrens, M., Jaïs, J.P., Travert, M., Lamant, L., Tournillac, O., Rousset, T., Fabiani, B., Cairns, R.A., et al. (2012). Recurrent TET2 mutations in peripheral T-cell lymphomas correlate with TFH-like features and adverse clinical parameters. Blood *120*, 1466–1469. https://doi.org/10.1182/BLOOD-2012-02-408542.

9. Sakata-Yanagimoto, M., Enami, T., Yoshida, K., Shiraishi, Y., Ishii, R., Miyake, Y., Muto, H., Tsuyama, N., Sato-Otsubo, A., Okuno, Y., et al. (2014). Somatic RHOA mutation in angioimmunoblastic T cell lymphoma. Nat. Genet. *46*, 171–175. https://doi.org/10.1038/ng.2872.

10. Lemonnier, F., Safar, V., Beldi-Ferchiou, A., Cottereau, A.-S., Bachy, E., Cartron, G., Fataccioli, V., Pelletier, L., Robe, C., Letourneau, A., et al. (2021). Integrative analysis of a phase 2 trial combining lenalidomide with CHOP in angioimmunoblastic T-cell lymphoma. Blood Adv. *5*, 539–548. https://doi.org/10.1182/BLOODADVANCES.2020003081.

11. Couronné, L., Bastard, C., and Bernard, O.A. (2012). TET2 and DNMT3A mutations in human T-cell lymphoma. N. Engl. J. Med. *366*, 95–96. https://doi.org/10.1056/NEJMC1111708/SUPPL_FILE/NEJMC1111708_DISCLOSURES.PDF.

12. Cairns, R.A., Iqbal, J., Lemonnier, F., Kucuk, C., De Leval, L., Jais, J.P., Parrens, M., Martin, A., Xerri, L., Brousset, P., et al. (2012). IDH2 mutations are frequent in angioimmunoblastic T-cell lymphoma. Blood *119*, 1901–1903. https://doi.org/10.1182/blood-2011-11-391748.

13. Mhaidly, R., Krug, A., Gaulard, P., Lemonnier, F., Ricci, J.E., and Verhoeyen, E. (2020). New preclinical models for angioimmunoblastic T-cell lymphoma: filling the GAP. Oncogenesis *9*, 73. https://doi.org/10.1038/s41389-020-00259-x.

14. Cortes, J.R., Ambesi-Impiombato, A., Couronné, L., Quinn, S.A., Kim, C.S., da Silva Almeida, A.C., West, Z., Belver, L., Martin, M.S., Scourzic, L., et al. (2018). RHOA G17V induces T follicular helper cell specification and promotes lymphomagenesis. Cancer Cell *33*, 259–273.e7. https://doi.org/10.1016/J.CCELL.2018.01.001.

15. Zang, S., Li, J., Yang, H., Zeng, H., Han, W., Zhang, J., Lee, M., Moczygemba, M., Isgandarova, S., Yang, Y., et al. (2017). Mutations in 5-methylcytosine oxidase TET2 and RhoA cooperatively disrupt T cell homeostasis. J. Clin. Invest. *127*, 2998–3012. https://doi.org/10.1172/JCI92026.

16. Ng, S.Y., Brown, L., Stevenson, K., DeSouza, T., Aster, J.C., Louissaint, A., and Weinstock, D.M. (2018). RhoA G17V is sufficient to induce autoimmunity and promotes T-cell lymphomagenesis in mice. Blood *132*, 935–947. https://doi.org/10.1182/blood-2017-11-818617.

17. Ward, P.S., Patel, J., Wise, D.R., Abdel-Wahab, O., Bennett, B.D., Coller, H.A., Cross, J.R., Fantin, V.R., Hedvat, C.V., Perl, A.E., et al. (2010). The common feature of leukemia-associated IDH1 and IDH2 mutations is a neomorphic enzyme activity converting α-ketoglutarate to 2-hydroxyglutarate. Cancer Cell *17*, 225–234. https://doi.org/10.1016/j.ccr.2010.01.020.

18. Figueroa, M.E., Abdel-Wahab, O., Lu, C., Ward, P.S., Patel, J., Shih, A., Li, Y., Bhagwat, N., Vasanthakumar, A., Fernandez, H.F., et al. (2010). Leukemic IDH1 and IDH2 mutations result in a hypermethylation phenotype, disrupt TET2 function, and impair hematopoietic differentiation. Cancer Cell *18*, 553–567. https://doi.org/10.1016/j.ccr.2010.11.015.

19. Lemonnier, F., Cairns, R.A., Inoue, S., Li, W.Y., Dupuy, A., Broutin, S., Martin, N., Fataccioli, V., Pelletier, R., Wakeham, A., et al. (2016). The IDH2 R172K mutation associated with angioimmunoblastic T-cell lymphoma produces 2HG in T cells and impacts lymphoid development. Proc. Natl. Acad. Sci. USA *113*, 15084–15089. https://doi.org/10.1073/pnas.1617929114.

20. Steinhilber, J., Mederake, M., Bonzheim, I., Serinsöz-Linke, E., Müller, I., Fallier-Becker, P., Lemonnier, F., Gaulard, P., Fend, F., and Quintanilla-Martinez, L. (2019). The pathological features of angioimmunoblastic T-cell lymphomas with IDH2 R172 mutations. Mod. Pathol. *32*, 1123–1134. https://doi.org/10.1038/s41379-019-0254-4.

21. Wang, C., McKeithan, T.W., Gong, Q., Zhang, W., Bouska, A., Rosenwald, A., Gascoyne, R.D., Wu, X., Wang, J., Muhammad, Z., et al. (2015). IDH2R172 mutations define a unique subgroup of patients with angioimmunoblastic T-cell lymphoma. Blood *126*, 1741–1752. https://doi.org/10.1182/BLOOD-2015-05-644591.

22. Li, J., Lu, E., Yi, T., and Cyster, J.G. (2016). EBI2 augments Tfh cell fate by promoting interaction with IL-2-quenching dendritic cells. Nature *533*, 110–114. https://doi.org/10.1038/nature17947.

23. Loghavi, S., Wang, S.A., Medeiros, L.J., Jorgensen, J.L., Li, X., Xu-Monette, Z.Y., Miranda, R.N., and Young, K.H. (2016). Immunophenotypic and diagnostic characterization of angioimmunoblastic T-cell lymphoma by advanced flow cytometric technology. Leuk. Lymphoma *57*, 2804–2812. https://doi.org/10.3109/10428194.2016.1170827.

24. Olatunde, A.C., Hale, J.S., and Lamb, T.J. (2021). Cytokine-skewed Tfh cells: functional consequences for B cell help. Trends Immunol. *42*, 536–550. https://doi.org/10.1016/j.it.2021.04.006.

25. Axelsson, S., Magnuson, A., Lange, A., Alshamari, A., Hörnquist, E.H., and Hultgren, O. (2020). A combination of the activation marker CD86 and the immune checkpoint marker B and T lymphocyte attenuator (BTLA) indicates a putative permissive activation state of B cell subtypes in healthy blood donors independent of age and sex. BMC Immunol. *21*, 1–9. https://doi.org/10.1186/s12865-020-00343-2.

26. Hsu, W.-C., Chen, M.-Y., Hsu, S.-C., Huang, L.-R., Kao, C.-Y., Cheng, W.-H., Pan, C.-H., Wu, M.-S., Yu, G.-Y., Hung, M.-S., et al. (2018). DUSP6 mediates T cell receptor-engaged glycolysis and restrains T FH cell differentiation. Proc. Natl. Acad. Sci. USA *115*, E8027–E8036. https://doi.org/10.1073/pnas.1800076115.

27. Wan, S., Ni, L., Zhao, X., Liu, X., Xu, W., Jin, W., Wang, X., and Dong, C. (2021). Costimulation molecules differentially regulate the ERK-Zfp831 axis to shape T follicular helper cell differentiation. Immunity *54*, 2740–2755.e6. https://doi.org/10.1016/j.immuni.2021.09.018.

28. Thibult, M.-L., Mamessier, E., Gertner-Dardenne, J., Pastor, S., Just-Landi, S., Xerri, L., Chetaille, B., and Olive, D. (2013). PD-1 is a novel regulator of human B-cell activation. Int. Immunol. *25*, 129–137. https://doi.org/10.1093/intimm/dxs098.

29. Kelly, L.M., Pereira, J.P., Yi, T., Xu, Y., and Cyster, J.G. (2011). EBI2 guides serial movements of activated B cells and ligand activity is detectable in lymphoid and non-lymphoid tissues. J. Immunol. *187*, 3026–3032. https://doi.org/10.4049/JIMMUNOL.1101262.

30. Laurent, C., Fazilleau, N., and Brousset, P. (2010). A novel subset of T-helper cells: follicular T-helper cells and their markers. Haematologica *95*, 356–358. https://doi.org/10.3324/haematol.2009.019133.

31. Kitano, M., Moriyama, S., Ando, Y., Hikida, M., Mori, Y., Kurosaki, T., and Okada, T. (2011). Bcl6 protein expression shapes pre-germinal center B cell dynamics and follicular helper T cell heterogeneity. Immunity *34*, 961–972. https://doi.org/10.1016/J.IMMUNI.2011.03.025.

32. Corneth, O., Mus, A.M., Asmawidjaja, P., Ouyang, W., Kil, L., Hendriks, R., Lubberts, E., and Lubberts, E. (2011). Impaired B cell immunity in IL-22 knock-out mice in collagen induced arthritis. Ann. Rheum. Dis. *70*, A58–A59. https://doi.org/10.1136/ARD.2010.149005.3.

33. Lee, A.Y.S., Reimer, D., Zehrer, A., Lu, M., Mielenz, D., and Körner, H. (2017). Expression of membrane-bound CC chemokine ligand 20 on follicular T helper cells in T–B-cell conjugates. Front. Immunol. *8*, 1871. https://doi.org/10.3389/FIMMU.2017.01871.

34. Bélanger, S., and Crotty, S. (2016). Dances with cytokines, featuring TFH cells, IL-21, IL-4 and B cells. Nat. Immunol. *17*, 1135–1136. https://doi.org/10.1038/ni.3561.

35. Keeley, E.C., Mehrad, B., and Strieter, R.M. (2010). CXC chemokines in cancer angiogenesis and metastases. Adv. Cancer Res. *106*, 91–111. https://doi.org/10.1016/S0065-230X(10)06003-3.

36. Protopsaltis, N.J., Liang, W., Nudleman, E., and Ferrara, N. (2019). Interleukin-22 promotes tumor angiogenesis. Angiogenesis *22*, 311–323. https://doi.org/10.1007/s10456-018-9658-x.

37. Benkheil, M., Van Haele, M., Roskams, T., Laporte, M., Noppen, S., Abbasi, K., Delang, L., Neyts, J., and Liekens, S. (2018). CCL20, a direct-acting pro-angiogenic chemokine induced by hepatitis C virus (HCV): potential role in HCV-related liver cancer. Exp. Cell Res. *372*, 168–177. https://doi.org/10.1016/j.yexcr.2018.09.023.

38. Do, H.T.T., and Cho, J. (2020). Involvement of the ERK/HIF-1α/EMT pathway in XCL1-induced migration of MDA-MB-231 and SK-BR-3 breast cancer cells. Int. J. Mol. Sci. *22*, 23–89. https://doi.org/10.3390/ijms22010089.

39. Song, Q., Shang, J., Zhang, C., Chen, J., Zhang, L., and Wu, X. (2020). Transcription factor RUNX3 promotes CD8+ T cell recruitment by CCL3 and CCL20 in lung adenocarcinoma immune microenvironment. J. Cell. Biochem. *121*, 3208–3220. https://doi.org/10.1002/JCB.29587.

40. Sekimata, M., Yoshida, D., Araki, A., Asao, H., Iseki, K., and Murakami-Sekimata, A. (2019). Runx1 and RORγt cooperate to upregulate IL-22 expression in Th cells through its distal enhancer. J. Immunol. *202*, 3198–3210. https://doi.org/10.4049/JIMMUNOL.1800672.

41. Sahoo, A., Alekseev, A., Tanaka, K., Obertas, L., Lerman, B., Haymaker, C., Clise-Dwyer, K., McMurray, J.S., and Nurieva, R. (2015). Batf is important for IL-4 expression in T follicular helper cells. Nat. Commun. *61*, 7997–8010. https://doi.org/10.1038/ncomms8997.

42. Robertson, K.D. (2002). DNA methylation and chromatin-unraveling the tangled web. Oncogene *21*, 5361–5379. https://doi.org/10.1038/sj.onc.

43. Razzaghi, R., Agarwal, S., Kotlov, N., Plotnikova, O., Nomie, K., Huang, D.W., Wright, G.W., Smith, G.A., Li, M., Takata, K., et al. (2021). Compromised counterselection by FAS creates an aggressive subtype of germinal center lymphoma. J. Exp. Med. *218*, e20201173. https://doi.org/10.1084/jem.20201173.

44. Zhang, J., Gao, J.X., Salojin, K., Shao, Q., Grattan, M., Meagher, C., Laird, D.W., and Delovitch, T.L. (2000). Regulation of FAS ligand expression during activation-induced cell death in T cells by p38 mitogen-activated protein kinase and C-jun nh2-terminal kinase. J. Exp. Med. *191*, 1017–1030. https://doi.org/10.1084/JEM.191.6.1017.

45. Dobay, M.P., Lemonnier, F., Missiaglia, E., Bastard, C., Vallois, D., Jais, J.-P., Scourzic, L., Dupuy, A., Fataccioli, V., Pujals, A., et al. (2017). Integrative clinicopathological and molecular analyses of angioimmunoblastic T-cell lymphoma and other nodal lymphomas of follicular helper T-cell origin. Haematologica *102*, e148–e151. https://doi.org/10.3324/HAEMATOL.2016.158428.

46. Suzuki, T., Miyoshi, H., Yanagida, E., Kawamoto, K., Yamada, K., Takeuchi, M., and Ohshima, K. (2019). Clinicopathological differences of nodal PTCL with Tfh phenotype from AITL and PTCL, NOS, and detection of prognostic marker of nodal PTCL with Tfh phenotype. Hematol. Oncol. *37*, 276–277. https://doi.org/10.1002/hon.87_2630.

47. Nguyen, T.B., Sakata-Yanagimoto, M., Asabe, Y., Matsubara, D., Kano, J., Yoshida, K., Shiraishi, Y., Chiba, K., Tanaka, H., Miyano, S., et al. (2017). Identification of cell-type-specific mutations in nodal T-cell lymphomas. Blood Cancer J. *7*, e516. https://doi.org/10.1038/BCJ.2016.122.

48. Notarangelo, G., Spinelli, J.B., Perez, E.M., Baker, G.J., Kurmi, K., Elia, I., Stopka, S.A., Baquer, G., Lin, J.-R., Golby, A.J., et al. (2022). Oncometabolite D-2HG alters T cell metabolism to impair CD8 + T cell function. Science *377*, 1519–1529. https://doi.org/10.1126/science.abj5104.

49. Bunse, L., Pusch, S., Bunse, T., Sahm, F., Sanghvi, K., Friedrich, M., Alansary, D., Sonner, J.K., Green, E., Deumelandt, K., et al. (2018). Suppression of antitumor T cell immunity by the oncometabolite (R)-2-hydroxyglutarate. Nat. Med. *24*, 1192–1203. https://doi.org/10.1038/S41591-018-0095-6.

50. Liu, Y., Wang, X., Deng, L., Ping, L., Shi, Y., Zheng, W., Lin, N., Wang, X., Tu, M., Xie, Y., et al. (2019). ITK inhibition induced in vitro and in vivo anti-tumor activity through downregulating TCR signaling pathway in malignant T cell lymphoma. Cancer Cell Int. *19*, 19–32. https://doi.org/10.1186/S12935-019-0754-9/FIGURES/6.

51. Delfau-Larue, M.H., de Leval, L., Joly, B., Plonquet, A., Challine, D., Parrens, M., Delmer, A., Salles, G., Morschhauser, F., Delarue, R., et al. (2012). Targeting intratumoral B cells with rituximab in addition to CHOP in angioimmunoblastic T-cell lymphoma. A clinicobiological study of the GELA. Haematologica *97*, 1594–1602. https://doi.org/10.3324/HAEMATOL.2011.061507.

52. Nechanitzky, R., Akbas, D., Scherer, S., György, I., Hoyler, T., Ramamoorthy, S., Diefenbach, A., and Grosschedl, R. (2013). Transcription factor EBF1 is essential for the maintenance of B cell identity and prevention of alternative fates in committed cells. Nat. Immunol. *148*, 867–875. https://doi.org/10.1038/ni.2641.

53. Sim, H.-W., Nejad, R., Zhang, W., Nassiri, F., Mason, W., Aldape, K.D., Zadeh, G., and Chen, E.X. (2019). Tissue 2-hydroxyglutarate as a biomarker for isocitrate dehydrogenase mutations in gliomas. Clin. Cancer Res. *25*, 3366–3373. https://doi.org/10.1158/1078-0432.CCR-18-3205.

54. Corces, M.R., Trevino, A.E., Hamilton, E.G., Greenside, P.G., Sinnott-Armstrong, N.A., Vesuna, S., Satpathy, A.T., Rubin, A.J., Montine, K.S., Wu, B., et al. (2017). An improved ATAC-seq protocol reduces background and enables interrogation of frozen tissues. Nat. Methods *14*, 959–962. https://doi.org/10.1038/NMETH.4396.

55. Béguelin, W., Teater, M., Meydan, C., Hoehn, K.B., Phillip, J.M., Soshnev, A.A., Venturutti, L., Rivas, M.A., Calvo-Fernández, M.T., Gutierrez, J., et al. (2020). Mutant EZH2 induces a pre-malignant lymphoma niche by reprogramming the immune response. Cancer Cell *37*, 655–673.e11. https://doi.org/10.1016/J.CCELL.2020.04.004.

56. Liao, Y., Smyth, G.K., and Shi, W. (2014). featureCounts: an efficient general purpose program for assigning sequence reads to genomic features. Bioinformatics *30*, 923–930. https://doi.org/10.1093/BIOINFORMATICS/BTT656.

57. Love, M.I., Huber, W., and Anders, S. (2014). Moderated estimation of fold change and dispersion for RNA-seq data with DESeq2. Genome Biol. *15*, 550. https://doi.org/10.1186/S13059-014-0550-8.

58. Buenrostro, J.D., Wu, B., Chang, H.Y., and Greenleaf, W.J. (2015). ATAC-seq: a method for assaying chromatin accessibility genome-wide. Curr. Protoc. Mol. Biol. *109*, 21–29. https://doi.org/10.1002/0471142727.MB2129S109.

59. Hatzi, K., Geng, H., Doane, A.S., Meydan, C., LaRiviere, R., Cardenas, M., Duy, C., Shen, H., Vidal, M.N.C., Baslan, T., et al. (2019). Histone demethylase LSD1 is required for germinal center formation and BCL6-driven lymphomagenesis. Nat. Immunol. *20*, 86–96. https://doi.org/10.1038/S41590-018-0273-1.

STAR★METHODS

KEY RESOURCES TABLE

REAGENT or RESOURCE	SOURCE	IDENTIFIER
Antibodies		
ANXV FITC	BD	556419; RRID: AB_2665412
B220 FITC (RA3-6B2)	BD	553088; RRID: AB_394618
B220 PeCy7 (RA3-6B2)	BD	552772; RRID: AB_394458
CD11b APC (M1/70)	BioLegend	101212; RRID: AB_312795
CD138 PE (281–2)	BioLegend	142504; RRID: AB_10916119
CD16/32 FcR block (2.4G2)	Tonbo Biosciences	70-0161; RRID: AB_2621487
CD19 APC Cy7 (6D5)	BioLegend	115530; RRID: AB_830707
CD25 APC Cy7 (PC61)	BioLegend	102026; RRID: AB_830745
CD25 APC (PC61)	BioLegend	102012; RRID: AB_312861
CD27 PerCP (LG.3A10)	BioLegend	124214; RRID: AB_2275577
CD3 APC Cy7 (145-2C11)	Thermo Fisher	25-0031-82; RRID: AB_469572
CD3 BV605 (17A2)	BioLegend	100237; RRID: AB_2562039
CD3 PE (145-2C11)	BioLegend	100308; RRID: AB_312673
CD3 PeCy7 (145-2C11)	Thermo Fisher	25-0031-82; RRID: AB_469572
CD38 APC (clone 90)	BioLegend	102712; RRID: AB_312933
CD4 BV605 (RM4-5)	BioLegend	100548; RRID: AB_2563054
CD4 FITC (GK1.5)	BioLegend	100406; RRID: AB_312691
CD4 PB (GK1.5)	BioLegend	100428; RRID: AB_493647
CD4 Pecy7 (RM4-5)	BioLegend	100528; RRID: AB_312729
CD4 PercP (RM4-5)	BioLegend	100540; RRID: AB_893326
CD40 FITC (cloneHM40-3)	BioLegend	102906; RRID: AB_312949
CD40L PE (MR1)	BioLegend	106506; RRID: AB_313271
CD62L FITC (MEL-14)	BioLegend	104406; RRID: AB_313093
CD69 PE (H1.2F3)	BioLegend	104508; RRID: AB_313111
CD8 APC (53–6.7)	BioLegend	100712; RRID: AB_312751
CD8 APC Cy7 (53–6.7)	BioLegend	100714; RRID: AB_312753
CD86 APC (clone GL1)	BioLegend	105012; RRID: AB_493342
cKit PeCy7 (2B8)	BioLegend	105814; RRID: AB_313223
Fas PE (Jo2)	BD	554258; RRID: AB_395330
FasL PE (MFL3)	BioLegend	106606; RRID: AB_313279
GI7 PB (GL-7)	Thermo Fisher	48-5902-82; RRID: AB_10870775
ICOS FITC (7E.17G9)	Thermo Fisher	11-9942-82; RRID: AB_11218290
ICOS PE (7E.17G9)	BioLegend	117406; RRID: AB_2122712
IgD FITC (11–26c.2a)	BD	553439; RRID: AB_394859
KI67 FITC (SolA15)	Thermo Fisher	11-5698-82; RRID: AB_11151330
Ly-6G/Ly-6C APC Cy7 (RB6-8C5)	BioLegend	108424; RRID: AB_2137485
Ly-6G/Ly-6C PeCy7 (M1/70)	BioLegend	101216; RRID: AB_312799
PD-1 APC (RMP1-30)	BioLegend	109112; RRID: AB_10612938
PDL1 PeCy7 (10F.9G2)	BioLegend	124314; RRID: AB_10643573
Sca1 PB (E13–161.7)	BioLegend	122520; RRID: AB_2143237
CD44 PE (IM7)	BioLegend	103008; RRID: AB_312959
B220 biotin	BioLegend	103204; RRID: AB_312989
CD11b biotin	BioLegend	101204; RRID: AB_312787
Cd11c biotin	BioLegend	117304; RRID: AB_313773

(*Continued on next page*)

Continued

REAGENT or RESOURCE	SOURCE	IDENTIFIER
CD19 biotin	BioLegend	115504; RRID: AB_313639
CD28 biotin (37.51)	BioLegend	102103; RRID: AB_312868
CD49 biotin	BioLegend	108904; RRID: AB_313411
CXCR5 biotin (2G8)	BD	551960; RRID: AB_394301
ICOSL biotin (HK5.3)	BioLegend	107403; RRID: AB_345259
Ly-6G/Ly-6C biotin	BioLegend	108404; RRID: AB_313369
NK1.1 biotin	BioLegend	108704; RRID: AB_313391
Ter199 biotin	BioLegend	116204; RRID: AB_313705
Streptavidin APC Cy7	BD	554063; RRID: AB_10054651
Streptavidin FITC	BD	554060; RRID: AB_10053373
Streptavidin PE	BD	554061, RRID: AB_1005332
Streptavidin PerCP	BD	554064; RRID: AB_2336918
CD3 (145-2C11)	BioLegend	100359; RRID: AB_2616673
CD28 (37.51)	BD Pharmigen	553294; RRID: AB_394763
IFNg	Peprotech	500-P119; RRID: AB_147751
IL-4	Peprotech	500-P54; RRID: AB_147635
TGFB (1D11)	R&D Systems	MAB1835; RRID: AB_357931
AffiniPure F(ab')$_2$ Fragment Goat Anti-Mouse IgM, μ chain specific	Jackson ImmunoResearch	115-006-020; RRID: AB_2338469
B220 (RA3-6B2)	BD	553086; RRID: AB_394616
CD138	BD	553712; RRID: AB_394998
CD4 (EPR19514)	Abcam	ab183685; RRID: AB_2686917
CD31	Abcam	ab28364; RRID: AB_726362
Pax5 (EPR3730)	Abcam	ab109443; RRID: AB_10862070
MUM1 (MUM1p)	Dako	M7259; RRID: AB_2127157
Biotinylated rabbit anti-goat	Vector Laboratories	BA-5000; RRID: AB_2336126
Biotinylated goat anti-mouse	Vector Laboratories	BA-9200;RRID: AB_2336171
Biotinylated goat anti-rabbit	Vector Laboratories	BA-1000; RRID: AB_2313606
5-methylcytosine (33D3)	Millipore	MABE146; RRID: AB_10863148
5-Hydroxymethylcytosine (5-hmC)	Active Motif	39769; RRID: AB_10013602
HIF1a	Novus Bio	NB100-105; RRID: AB_10001154
VEGFR2	Abcam	ab115805; RRID: AB_10899278
anti-rabbit HRP	Agilent	K4003; RRID: AB_2630375
anti-mouse HRP	Agilent	K4001; RRID: AB_2827819
Ultra-LEAF™ Purified Rat IgG2b, κ Isotype Ctrl Antibody	BioLegend	400601; RRID: AB_326545
InVivoMAb polyclonal Armenian hamster IgG	BioXCell	BE0091; RRID: AB_1107773
Ultra-LEAF™ Purified anti-mouse CD86 Antibody	BioLegend	105052; RRID: AB_2832340
Ultra-LEAF™ Purified anti-mouse CD80 Antibody	BioLegend	600053; RRID: AB_2910468
InVivoMAb anti-mouse PD-1 (CD279)	BioXCell	BE0273; RRID: AB_2687796
InVivoMAb anti-mouse CD40L (CD154)	BioXCell	BE0017-1; RRID: AB_1107601
Ultra-LEAF™ Purified anti-mouse CD278 (ICOS) Antibody	BioLegend	117413; RRID: AB_2832411
Purified Hamster Anti-Mouse CD95	BD	554255; RRID: AB_395327
Phospho-Src Family (Tyr416) Antibody	Cell signaling	2101; RRID: AB_331697
Src Antibody	Cell signaling	2108; RRID: AB_331137
Phospho-Zap-70 (Tyr319)/Syk (Tyr352) (65E4)	Cell signaling	2717; RRID: AB_2218658
Zap-70 (D1C10E) XP®	Cell signaling	3165; RRID: AB_2218656
Phospho-PLCγ1 (Tyr783) Antibody	Cell signaling	2821; RRID: AB_330855

(*Continued on next page*)

Continued

REAGENT or RESOURCE	SOURCE	IDENTIFIER
PLCγ1 Antibody	Cell signaling	2822; RRID: AB_2163702
Phospho-SAPK/JNK (Thr183/Tyr185) (G9)	Cell signaling	9255; RRID: AB_2307321
SAPK/JNK Antibody	Cell signaling	9252; RRID: AB_2250373
Phospho-p44/42 MAPK (Erk1/2) (Thr202/Tyr204) (E10)	Cell signaling	9106; RRID: AB_331768
p44/42 MAPK (Erk1/2) Antibody	Cell signaling	9102; RRID: AB_330744
Phospho-Akt (Ser473) (D9E) XP® Rabbit mAb	Cell signaling	4060; RRID: AB_2315049
Akt (pan) (40D4)	Cell signaling	2920; RRID: AB_1147620
Phospho-NF-κB p65 (Ser536) (93H1) Rabbit mAb	Cell signaling	3033; RRID: AB_331284
NF-κB p65 (L8F6) Mouse mAb	Cell signaling	6956; RRID: AB_10828935
Phospho-p38 MAPK (Thr180/Tyr182) (3D7) Rabbit mAb	Cell signaling	9215; RRID: AB_331762
p38 MAPK Antibody	Cell signaling	9212; RRID: AB_330713
Vinculin (E1E9V) XP® Rabbit mAb	Cell signaling	13901; RRID: AB_2728768
IRDye® 680RD Goat anti-Mouse IgG Secondary Antibody	LI-COR	926–68070, RRID: AB_10956588
IRDye® 680RD Goat anti-Rabbit IgG Secondary Antibody	LI-COR	926–68071; RRID: AB_10956166
IRDye® 800CW Goat anti-Mouse IgG Secondary Antibody	LI-COR	926–32210; RRID: AB_621842
IRDye® 800CW Goat anti-Rabbit IgG Secondary Antibody	LI-COR	926–32211; RRID: AB_621843
Chemicals, peptides, and recombinant proteins		
ImmPACT® DAB	Vector	SK-4105
7AAD	BioLegend	420404
DAPI	Sigma	D9542
Digitonin	Promega	G9441
Fetal Bovine Serum	Multicell	98150
Fixable viability dye eFluor 780	Thermo Fisher	65-0865-18
Immobillon Crescendo Western HRP Substrate	Millipore	WBLUR0100
L-glutamine	Multicell	609-065-EL
LZ-hFasL	gifted by Pr S. Nagata	
Penicillin Streptomycin	Multicell	450-201-EL
Recombinant Mouse IL21	Peprotech	210–21
Recombinant Mouse IL6	Peprotech	216–16
RPMI medium 1640	Life Technologies	61870044
Sheep Red Blood cells	Cocalico Biologicals Inc	20–1334A
Sodium pyruvate	Multicell	600-110-EL
Enasidenib (AG-221)	Selleckchem	S8205
CellTrace™ Violet Cell Proliferation Kit	Invitrogen	C34557
Intercept® (TBS) Blocking Buffer	LI-COR	927–60001
HIER citrate buffer pH6.0 at 1X	Zytomed	ZUC028-500
BLOXALL® Endogenous Blocking Solution	Vector	SP-6000
Protein Block Serum-Free	Dako	X0909
Antibody diluent	Dako	S2022
Vectamount aquouse medium	Vector	H-5501
PBS solution	Wisent	311–010
4X Bolt LDS Sample Buffer	Thermo Fisher	B0007

(*Continued on next page*)

Continued

REAGENT or RESOURCE	SOURCE	IDENTIFIER
10X Bolt Sample Reducing Agent	Thermo Fisher	B0009
Bolt 4–12% Bis-Tris Plus gels	Thermo Fisher	NW04120BOX
BioTrace NT nitrocellulose membrane for western blot	PALL Life Sciences	66485
Immobilon PVDF membrane for western blot	Millipore	IPFL00010
20X Bolt MES SDS Running Buffer	Thermo Fisher	B0002
20X Bolt Transfer Buffer	Thermo Fisher	BT0006
CelLytic™ M	Sigma-Aldrich	C2978
PhosphoSTOP	Sigma-Aldrich	4906837001
Pierce™ Protease Inhibitor Mini Tablets, EDTA-free	Fisher	A32955
Critical commercial assays		
AllPrep DNA/RNA Micro Kit	Qiagen	80284
Cytofix/Cytoperm kit	BD Biosciences	554714
IgG (Total) Mouse Uncoated ELISA Kit with Plates	Invitrogen	88–50400
MinElute Reaction Cleanup	Qiagen	28004
Mouse Lineage Cell Depletion Kit	Miltenyi Biotec	130-090-858
Mouse Vβ TCR screening panel	BD Biosciences	557004
Naive $CD4^+$ T cell Isolation Kit	Miltenyi Biotec	130-104-453
Nextera DNA LibraryPrep Kit	Illumina	FC-121-1030
Nucleospin RNAPlus	Macherey Nagel	740984
Nucleospin Tissue Kit	Macherey Nagel	740901
Streptavidin Particles Plus - DM	BD Biosciences	557812
Taq DNA Polymerase	Fermantas	EP0404
eBioscience™ Foxp3/Transcription Factor Staining Buffer Set	Thermo Fisher	00-5523-00
D-2-Hydroxyglutarate (D2HG) Assay Kit	Sigma	MAK320
BCA™ protein Assay Kit	Thermo Fisher	23227
Deposited data		
5mC-seq - sequencing data	This manuscript	GSE221604
ATAC seq- sequencing data	This manuscript	GSE221602
RNAseq- sequencing data	This manuscript	GSE221600
Human data Affymetrix	Dobay, 2017[45]	
RNA seq tissue - sequencing data	This manuscript	GSE221599
Experimental models: Organisms/strains		
B6.129S2-Tcratm1Mom/J	The Jackson Laboratory	#002116
Tg(Cd4-cre)1Cwi/BfluJ	The Jackson Laboratory	#17336
B6.Cg-Gt(ROSA)26Sortm14 (CAG-tdTomato)Hze/J	The Jackson Laboratory	#7914
B6(Cg)-Tet2tm1.2Rao/J	The Jackson Laboratory	#023359
B6.SJL-Ptprca Pepcb/BoyJ	The Jackson Laboratory	#002014
$Idh2^{LSL-R172K}$	Lemonnier et al., 2018	NA
NOD.Cg-Prkdcscid Il2rgtm1Wjl/SzJ	The Jackson Laboratory	#005557
Human samples		
Human AITL tumor samples – Affymetrix	Dobay, 2017[45]	
Human AITL tumor samples – FFPE blocks	Dr. Philippe Gaulard's laboratory, TENOMIC consortium	N/A

(*Continued on next page*)

Continued

REAGENT or RESOURCE	SOURCE	IDENTIFIER
Human AITL tumor samples – Nanostring study	Dr. Philippe Gaulard's laboratory, TENOMIC consortium	N/A
Software and algorithms		
Flowjo 10.2	Flowjo	https://www.flowjo.com/solutions/flowjo
Prism software v7.3	Graphpad	https://www.graphpad.com/scientificsoftware/prism/
ImmunoSEQ analyzer	Adaptive Biotechnologies	
FASTQC v0.11.5	Babraham Bioinformatics	https://www.bioinformatics.babraham.ac.uk/projects/fastqc/
MultiQC v0.8	Ewels et al., 2016	
STAR aligner v2.5.2b	Liao et al., 2014[56]	
DESeq2 R package v1.20.0	Love et al., 2014[56]	
NDP.view2 imaging software	Hamamatsu	
fastp v0.20.1		https://www.bioinformatics.babraham.ac.uk/projects/fastqc/).
Other		
5mC-seq	Weill Cornell Medicine Epigenomics Core at Weill Cornell Medicine	
ATAC-seq	Weill Cornell Medicine Epigenomics Core at Weill Cornell Medicine	
RNA-seq	Weill Cornell Medicine Epigenomics Core at Weill Cornell Medicine	
Mouse immunoSEQ assay	Adaptive Biotechnologies, (Seattle, USA)	
RNAseq from tissue	Novogene Co. Ltd. (Beijing, China)	

RESOURCE AVAILABILITY

Lead contact

Further information and requests for resources and reagents should be directed to and will be fulfilled by the lead contact, Tak Wah Mak (Tak.Mak@uhnresearch.ca).

Materials availability

There are restrictions to the availability of any mouse model material due to the Materials Transfer Agreement with Agios Pharmaceuticals for the *Idh2*^{R172K} mouse.

Data and code availability

- All bisulfite-seq, ATAC-seq and RNA-seq data have been deposited at GEO and are publicly available as of the date of publication of this paper. Accession numbers are listed in the key resources table. This paper also analyzes existing, publicly available data (Dobay et al. 2017).[45]
- This paper does not report original code.
- Any additional information required to reanalyze the data reported in this paper is available from the lead contact upon request.

EXPERIMENTAL MODEL AND SUBJECT DETAILS

Mice

The *Idh2*$^{LSL-R172K}$ conditional knock-in allele was generated previously.[19] The mouse strains *Tet2*$^{f/f}$ [B6(Cg)-Tet2tm1.2Rao/J, #023359], *Cd4*-Cre [Tg(Cd4-cre)1Cwi/BfluJ #017336], *TCRa* KO (B6.129S2-Tcratm1Mom/J, #002116) and *tdTomato* [B6.Cg-Gt(ROSA)26Sortm14(CAG-tdTomato)Hze/J, #007914] were all from The Jackson Laboratory and backcrossed to C57BL/6J mice for at least 10 generations. Mice were maintained under specific pathogen-free conditions and housed in temperature-controlled facilities under 12-h light/12-h dark conditions with access to food and water *ad libitum* at the Animal Resource Center of the Princess Margaret Hospital (PMH; part of UHN, Toronto, Canada). Littermates (2–8 months old) carrying appropriate genotype(s) were randomly assigned to experimental groups. Male and female animals were used in this study. All animal experiments were performed according to institutional and federal guidelines, and were approved by the PMH Animal Care Committee (protocols #985 and #6503).

For the AT model, recipient mice developing malocclusion or rectal prolapse were excluded from the analyses. For survival curves, AT mice were observed until age 80 weeks. For all other analyses, sick AT mice were analyzed at the humane endpoint (moribund state), and healthy AT mice at the experimental time limit of 45 weeks.

Tumor transplantation into NSG mice

NOD.Cg-Prkdcscid Il2rgtm1Wjl/SzJ (NSG) mice were obtained from The Jackson Laboratory (#005557) and housed in the PMH Animal Resource Center. Single-cell suspensions derived from tumors or spleens were prepared in PBS and injected intravenously (5×10^6 cells per NSG mouse). Alternatively, 6–8 week old NSG mice were anesthetized with Ketamine/Xylazine prior to subcutaneous transplantation of a $3mm^2 \times 3mm^2$ tumor fragment from a sick P/S t*Tet2* or P/S t*Idh2*;*Tet2* mouse. Recipient mice were checked every week and sacrificed when they became sick and splenomegaly was palpable (humane endpoint, usually, 30–60 days post-transplantation). Fragments of liver, spleen and lung were collected for histological study, and single-cell suspensions of spleen cells were prepared for FACS analysis.

Human AITL studies

The Dobay cohort[45] included 72 AITL patients for whom *IDH2* mutational status and gene expression profiles were available. Tumor samples had been analyzed using Affymetrix HGU133 Plus 2.0 microarrays. Among these patients, 51 were $IDH2^{WT}$ (22 were *TET2*-mutated, 24 were *TET2*-WT and 5 undetermined), and 21 were $IDH2^{R172}$ (15 were *TET2*-mutated and 6 were *TET2*-WT).

For analysis of TME and Nanostring studies, samples were from a cohort of 77 AITL patients who had been included in the previous RAIL and REVAIL clinical trials,[10,51] and for whom mutational status was determined by next generation sequencing. Among these patients, 58 were $IDH2^{WT}$ (41 were *TET2*-mutated, 15 were *TET2*-WT and 2 undetermined), and 19 were $IDH2^{R172}$ (18 were *TET2*-mutated and 1 was undetermined). IHC analyses were conducted on samples from a few patients from this cohort ($IDH2^{WT}$ AITL: n = 8/9 and $IDH2^{R172K}$ AITL: n = 7/9). These patient samples were collected with informed consent through the TENOMIC consortium as approved by the Ethical Committee CPP Ile-de-France (protocol #08–009). All samples were examined by experienced pathologists.

METHODS DETAILS

Mouse cell isolation

Mice were euthanized and single-cell suspensions were prepared. For spleen and LNs, tissues were crushed in cold buffer (PBS 1X without $MgCl_2$ or $CaCl_2$, supplemented with 0.5% BSA, 2mM EDTA pH8.0). For BM, cells were isolated by flushing marrow with buffer using syringes with 26 gauge needles. Cell pellets were resuspended in red blood cell lysis buffer (Sigma #R7757) and incubated for 8 min at room temperature (RT). Cells were counted on a ViCell Counter and resuspended at a dilution appropriate for each experiment.

The Naive $CD4^+$ T cell Isolation Kit (Miltenyi Biotec #130-104-453) was used to isolate $CD4^+$ T cells from spleens and LNs of 2/3-month-old GEMM mice. The Mouse Lineage Cell Depletion Kit (Miltenyi Biotec #130-090-858) was used to enrich for lineage-negative cells from BM. The manufacturer's instructions were followed in both cases. $CD3^+$ T cells were isolated from spleens and LNs by negative selection using biotin-coupled antibodies: anti-CD19 (Biolegend #115504), anti-B220 (Biolegend #103204), anti-Ter119 (Biolegend #116204), anti-NK1.1 (BioLegend #108704), anti-CD49b (Biolegend #108904), anti-Ly-6G/Ly-6C (Biolegend #108404), anti-CD11b (Biolegend #101204), and anti-CD11c (BioLegend #117304), followed by incubation with Streptavidin Particles Plus-DM (BD, #557812) according to the manufacturer's instructions. The purity of isolated cells was assessed by flow cytometry.

Adoptive T cell transfer to generate AT strains and GC reaction induction *in vivo*

$CD3^+$ T cells were isolated from each of the 4 GEMM strains (2/3 months old) as described above and transplanted (1×10^6/mouse) by intraperitoneal injection into 8-week-old *TCRa* KO recipient mice to generate the corresponding AT strains. To induce robust Tfh cell development and generate GC responses in these recipients, AT mice were immunized with 1×10^9 sheep red blood cells at 48 h post-transplant (SRBC; Cocalico Biologicals Inc, #20–1334A) in 500μL PBS delivered by intraperitoneal injection, with injections repeated every 3 weeks until the experimental endpoint was reached. Control mice were injected with PBS.

Flow cytometry and antibodies

For surface staining, cells were pre-incubated for 15 min at 4°C with Fc blocking antibody (Tonbo Biosciences # 70-0161-M001) and stained with the appropriate antibodies for 30 min at 4°C. For intracellular staining to detect Ki67, and after surface staining, cells were fixed and permeabilized using the eBioscience Foxp3/Transcription Factor Staining Buffer Set (Thermo; #00-5523-00). All stained cells were examined using a Fortessa 1 Flow Cytometer (BD Biosciences). Analysis of FACS data was performed using FlowJo Software.

Cell proliferation

$CD4^+$ T cells (1×10^5) were isolated from 2/3-month-old GEMM mice and activated by culture on plates coated with various concentrations of anti-mouse CD3e antibody (BD Pharmingen, # 553294) in the presence of soluble anti-mouse CD28 antibody

(1 μg/mL; BD Pharmingen, #553294) for 48 h and pulsed for the last 8 h with [^{3}H]-thymidine (1μCi/well). Incorporation of [^{3}H]-thymidine was measured using a Matrix 96 Direct β Counter System (Canberra Packard).

For co-culture experiments, B cell proliferation was determined using Cell Trace Violet (Invitrogen, #C34557) according to the manufacturer's instructions. For CD3$^+$ T cells transplanted into AT mice, cells were stained with Ki67 and analyzed by FACS analysis at 7 days post-transplant.

In vitro Tfh cell differentiation

Tfh cell differentiation experiments were performed following procedures described by Cortes et al.[14] Briefly, naive CD4$^+$ T cells were isolated from 2/3-month-old GEMM mice and co-cultured with irradiated T cell-depleted splenocytes as co-stimulator cells (ratio 5:1) on anti-CD3-coated plates containing RPMI supplemented with 25 ng/mL IL-6 (#216–16, Peprotech), 50 ng/mL IL-21 (#210–21, Peprotech), 4 ng/mL anti-IFNγ (#500-P119, Peprotech), 4 mg/mL anti-IL-4 (#500-P54, Peprotech), and 20 mg/mL anti-TGFβ (#1D11, R&D Systems). After 72 h, Tfh cell markers were evaluated by staining with anti-ICOS, anti-PD-1, and anti-CXCR5 antibodies followed by flow cytometry.

Detection of TCR signaling

CD4$^+$ T cells were isolated from spleens and LNs of a pool of five 2/3-month-old GEMM mice per group by negative selection using biotin-coupled antibodies as described above. T cells (1 × 10^7) were activated by culture on 6-well plates coated with 3 μg/mL anti-CD3e antibody (BD Pharmingen, # 553294) for 3 min, 10 min, 30 min or 45 min at 37°C. T cells were then washed with cold PBS and frozen in liquid nitrogen prior to examination by immunoblotting.

Co-culture of Tfh cells and B cells

CD19$^+$ cells (5 × 10^4) and Tfh cells (3 × 10^4) that had been isolated from 2/3-month-old GEMM mice using a FACSAria Fusion fluorescence-activated cell sorter (BD Biosciences, purity >98%) were seeded in anti-CD3-coated 96-well round bottom plates in RPMI 1640 supplemented with 1% L-glutamine, 10% heat-inactivated fetal calf serum (hFCS), 1% penicillin/streptomycin, 1% sodium pyruvate, 0.1% beta-mercaptoethanol, and 5 μg/mL anti-IgM. Cultures were incubated at 37°C for 6 days without replenishment of the culture medium prior to analysis.

FasL-induced apoptosis

Recombinant FasL protein was generously provided by Professor Shigekazu Nagata (Immunology Frontier Research Center, Osaka University, Japan). For FasL treatment, splenocytes from AT mice were resuspended at 2 × 10^6 cells/200 μL in RPMI 1640 supplemented with 10% FCS and incubated for 2 h at 37°C in 5% CO_2 with 0–35 laboratory units of recombinant FasL protein. One laboratory unit corresponded to the concentration of FasL that gave half-maximal cytotoxicity against 7.5 × 10^4 cells (WR19L) in 100 μL. FasL-treated cells were stained with Annexin-7AAD and analyzed by FACS to detect apoptosis (see below). Thymocytes of a young WT mouse were analyzed in parallel as a positive control.

Annexin-7AAD staining

To determine cell viability and apoptosis at the end of an *in vitro* experiment, cells were collected, stained to detect surface markers, resuspended in Annexin-V buffer (ANXV, 0.01M HEPES pH 7.4, 0.14M NaCl, 2.5mM $CaCl_2$) containing ANXV-FITC antibody (BD, #556419) plus 7AAD, and incubated at RT for 30 min before analysis by flow cytometry.

Blocking antibodies and IDHi *in vitro* assays

Co-cultures of Tfh cells and WT B cells were established as described above. On day 1 of co-culture, various blocking antibodies were added: either isotype control; or anti-CD80 (5 μg/mL) and anti-CD86 (5 μg/mL); or anti-PD-1 (20μg/mL); or anti-CD40L (20μg/mL); or anti-ICOS (5 μg/mL); or anti-Fas (5 μg/mL); or Enasidenib (IDH2 inhibitor; Selleckchem, #S8205, 1 μM). After 4 days at 37°C, B cell survival and proliferation were assayed as described above.

Histology and immunohistochemistry

Mouse tissues were fixed in formaldehyde, transferred into 70% ethanol and embedded in paraffin using a HistoCore Arcadia H instrument (Leica) before 4.5 mm sections were cut on an RM2255 instrument (Leica). Staining with hematoxylin and eosin (H&E) was performed on paraffin-embedded tissue sections using a Leica ST5010 AutoStainer XL.

Immunohistochemical analyses of mouse tissues were performed using anti-mouse antibodies against CD4 (#ab183685, Abcam), B220 (#553086, BD), CD138 (#553712, BD Pharmingen), CD31 (#ab28364, Abcam), Pax5 (#ab109443, Abcam) and MUM1 (#M725901, Dako). The appropriate secondary antibodies (Amersham/GE Healthcare) were applied and DAB HRP substrate solution (Vector Laboratories), prepared according to the manufacturer's instructions, was applied for 3 min. Sections were counterstained with hematoxylin, dehydrated in graded ethanol and xylene series, and mounted. Histology slides were scanned using a NanoZoomer 2.0 HT instrument at 20X magnification.

For immunohistochemical analyses of FFPE-prepared tumor tissue samples from AITL patients, paraffin-embedded tissue sections of 2.5 μm were de-paraffinized and subjected to antigen retrieval (Dako). Endogenous peroxidase activity was quenched with BLOXALL Endogenous Blocking Solution (#SP-6000, Vector) for 10 min in a humid room. Sections were then blocked with

Protein Block Serum-Free (#X0909, Dako) for 10 min. Slides were incubated with primary antibody diluted with Antibody Diluent (#S2022, Dako), washed, and incubated for 30 min with HRP-conjugated anti-rabbit or anti-mouse antibody (#K4003 or K4001, Dako). Slides were counterstained with hematoxylin and mounted using Vectamount Aqueous Medium (# H-5501, Vector). Images were captured at 20X magnification using an Aperio Digital Pathology Slide Scanner; ScanScope XT (Leica).

Staining intensity

Staining intensity of tissue sections was quantified using QuPath software v0.2.3 downloaded from the QuPath homepage located at Github (https://qupath.github.io/). For each patient sample, 5 representative regions of interest (ROI) of equivalent surface area were analyzed. The number of blood vessels per region was determined by QuPath, and the mean of these values for all regions was used to determine the number of vessels per sample.

T cell clonality

TCR Vβ repertoire analysis of DNA samples from LNs was performed by Adaptive Biotechnologies (Seattle, USA) using high-throughput sequencing and a proprietary mouse immunoSEQ assay. Data were analyzed using Adaptive Biotechnologies immunoSEQ analyzer proprietary software. Alternatively, TCR-β clonality of $CD4^+$ T cells was determined by combining surface marker staining with use of the Mouse Vβ TCR screening panel kit (BD Biosciences; #557004), which contains FITC-labelled monoclonal antibodies recognizing TCR β2, β3, β4, β5.1, β6, β7, β8.1, β8.3, β9, β10, β11, β12, β13, β14, or β17.

B cell clonality

VDJ recombination analysis was assessed by subjecting 1 μg of spleen DNA to PCR (#EP0404, Fermantas) using specific primers as previously described.[52] PCR products were analyzed by standard agarose gel electrophoresis. Isolated $CD19^+$ cells were used as a positive control, and the PCR mix without DNA was used as the negative control.

IgG levels

IgG levels in mouse serum or cell culture supernatants were evaluated using an ELISA kit (#88–50400, Invitrogen) according to manufacturer's instructions. Serum samples were diluted 1/10,000 before assay. Culture supernatants were not diluted.

D2HG levels

Measurements of D2HG in mouse peripheral blood (20 μL), or in cells (5×10^5) isolated from mice using a FACSAria Fusion fluorescence-activated cell sorter (BD Biosciences, purity >98%), were performed by HPLC-MS/MS as previously described.[53]

Measurements of D2HG in culture supernatants were performed using a D-2-Hydroxyglutarate Assay Kit according to the manufacturer's instructions (MAK320, Sigma). All cells in a co-culture were counted on a ViCell Counter to normalize assay results. Concentration of D2HG is given in pmol per mL of supernatant. Measurements of intracellular levels of D2HG in co-cultured cells were determined by separating T and B cells by negative selection with biotin-coupled antibodies as described above. Separated cells were counted on a ViCell Counter, lysed using CelLytic M (Sigma-Aldrich, C2978), and assayed for intracellular D2HG using the same kit and protocol. Intracellular D2HG levels are expressed in pmol per 1×10^6 cells.

Immunoblotting

T cells activated as above were lysed by incubation at 4°C for 30 min with constant agitation in NP-40 buffer (20mM Tris HCl pH8, 137mM NaCl, 10% glycerol, 0.5% NP-40, 2.5mM EDTA) supplemented with 1 tab of PhosphoSTOP (Sigma-Aldrich, #4906837001) and 1 tab of protease inhibitor (Fisher, #A32955). After centrifugation and quantification using a BCA kit (Thermo Fisher, #23227), cell lysate protein samples (70μg) were prepared using 1X Bolt LDS Sample Buffer (Thermo Fisher #B0007) plus 1X Bolt Sample Reducing Agent (Thermo Fisher #B0009), and incubated at 70°C for 10 min with constant motion. Samples were separated on Bolt 4–12% Bis-Tris Plus gels (Thermo Fisher, #NW04120BOX using Bolt MES SDS Running Buffer), and transferred onto nitrocellulose membranes (BioTrace NT, PALL Life Sciences #66485) in Bolt Transfer Buffer (Thermo Fisher, #BT006) for 1 h at 10 V at RT following the manufacturer's instructions. Membranes were blocked for 1 h at RT with blocking solution (LI-COR, #927–60001). Proteins were immunoblotted by incubation with the appropriate primary antibodies overnight at 4°C in blocking buffer +0.1% Tween. Membranes were washed three times in TBST (TBS 1x + 0.01% Tween), incubated for 1 h at RT with secondary antibodies in blocking buffer +0.2% Tween, and washed three times in TBST. Fluorescence detection was performed with an Odyssey CLx instrument (LI-COR).

Dot blots

Cells (1×10^6) were isolated from spleens and LNs of GEMM mice using a FACSAria Fusion fluorescence-activated cell sorter (BD Biosciences, purity >98%) and genomic DNA was extracted using the Nucleospin Tissue kit (#740901, Macherey-Nagel). Genomic DNA was denatured in 0.4 M NaOH, 10mM EDTA at 100°C for 10 min, followed by neutralization with chilled 0.2 M Tris-HCl (pH 8.0). 2-fold serial dilutions of denatured genomic DNA were blotted onto Hybond N+ membranes (Amersham #RPN119B) using a BIO-DOT apparatus (Bio-Rad). After washing with SSC 2x buffer, membranes were dried, cross-linked (1200 μJ/cm2) with a UV Stratalinker 2400 (Stratagene), blocked, and incubated overnight at 4°C with anti-5hmC (#39769, Active Motif) or anti-5mC (#MABE146, Millipore) antibody. Chemiluminescence detection was performed using Immobilon Crescendo Western HRP Substrate (Millipore #WBLUR0100) and a Micro-Chemi 4.2 instrument (Bio-Imaging Systems).

Preparation of samples for bulk RNA-seq, bisulfite-seq and ATAC-seq

$CD3^+$ T cells were isolated from spleen and LNs of 2/3-month-old mice by negative selection as described above. Viable Tfh cells ($CD4^+CXCR5^+PD\text{-}1^+$) were sorted using a FACSAria II or FACSAria Fusion fluorescence-activated cell sorter (BD Biosciences, purity >98%).

For ATAC-seq samples, the OMNI-ATAC method was used as previously described.[54] Briefly, viable Tfh cells (5×10^4) were collected and resuspended in ATAC-Resuspension Buffer (RSB) containing 0.1% NP40, 0.1% Tween 20, and 0.01% digitonin. After washing in RSB containing 0.1% Tween 20, pellets were incubated at 37°C for 30 min in transposition reaction mix using the Nextera DNA LibraryPrep Kit (#FC-121-1030, Illumina). Clean-up of transposed fragments was performed using MinElute Reaction Cleanup (#28004, Qiagen) according to the manufacturer's protocol.

For bulk RNA-seq and bisulfite-seq samples, viable Tfh cells (2.5×10^5) were collected and both DNA and RNA were extracted using the AllPrep DNA/RNA Micro Kit (Qiagen #80284) following the manufacturer's instructions.

Transcriptomic analysis

For Tfh cells, total RNA was extracted from Tfh cells (2.5×10^5) as described above. RNA quality was evaluated using an Agilent Technologies 2100 Bioanalyser. Library preparation, sequencing and post-processing of raw data were performed by the Weill Cornell Medicine Epigenomics Core at Weill Cornell Medicine using Truseq RNA sample kits (Illumina) on an Illumina HiSeq 2500 instrument as previously described.[55] The STAR aligner (v2.5.1b) was used to map fastq files to the reference genome mm10.[56] DESeq2 was used to perform differential gene expression analysis comparing mutant to WT samples.[57] The significance threshold for differential gene expression was set at fold-change>1.58 and $q < 0.01$ after adjusting for multiple testing using the Benjamini-Hochberg correction.

For LN tissues (healthy or tumoral), total RNA was extracted using a Nucleospin RNAPlus kit (#740984.250, Macherey Nagel). Libraries were prepared and sequenced by Novogene Co. Ltd. (Beijing, China) using an Illumina NovaSeq 6000 Sequencing System.

Oxidative reduced representation bisulfite sequencing

Genomic DNA was subjected to Oxidative Reduced Representation Bisulfite Sequencing (oxRRBS). Librairies were merged, and NuGEN adapters (R1: AGATCGGAAGAGC; R2: AAATCAAAAAAAC) were trimmed according to the following parameters: -l 2 -Q –trim_poly_g –overrepresentation_analysis (fastp v0.20.1). The sequencing reads were aligned to the mm10 genome build (bwa-meth v0.2.2, default mapping parameters), and binary alignment maps were established using Sambamba v0.7.0. Estimated 5-methylcystosine (5mC) values were established using MethylDackel v0.3.0-3-g084d926 plus HTSlib v1.2.1 (with default scoring parameters) and merged with MethylDackel. A custom Python script was used to transform the output files (in bedGraph format) into MethylKit format. These values were combined into a global matrix, normalized (methylKit v1.12.0), and filtered for the X and Y chromosomes and mitochondria. A subtractional approach between bisulfite and oxidative-bisulfite values (approach via MLML2R, https://doi.org/10.1515/sagmb-2018-0031) was set up to obtain estimated 5-hydroxymethylcytosine (5hmC) values. However, this analysis was discarded due to inconsistent results. Differential methylation was determined using methylKit, with the significance threshold set to a minimum methylation difference of 10% and $q < 0.01$.

ATAC-sequencing

Samples were prepared as above and ATAC-sequencing was performed using the Omni-ATAC protocol as described.[58] ATAC-seq DNA libraries were generated and sequenced on a Hi-Seq 2500 instrument (Illumina). ATAC-seq reads were processed and analyzed following a previously described pipeline.[59] DESeq2 was used to identify differentially accessible peaks. Peaks were annotated using the mm10 reference genome build as promoters (+/− 5kb of TSS) and regulatory regions. The significance threshold to determine differential peaks was set at $q < 0.01$.

Nanostring gene expression profiling

Gene expression profiling of AITL patient samples was performed using the nCounter PanCancer IO 360 Panel (NanoString Technologies, Seattle, Washington), which includes 770 genes involved in the main biological pathways of human immunity. Experiments were performed by the staff of the Genomics Platform of the Institut Curie (Paris, France). For each sample, 500 ng total RNA extracted from a formalin-fixed, paraffin-embedded tumor block was used as the template. A human Universal Reference RNA sample, which included a no-template control (water) and 10 positive control cell lines, was hybridized in parallel with the tumor samples of interest. Nanostring positive and negative controls were also added to samples. Probes and mRNAs were hybridized overnight at 65°C, followed by processing using the NanoString nCounter preparation station (NanoString Technologies) to immobilize biotinylated hybrids on a cartridge coated with streptavidin, and to remove excess probe. The nCounter Digital Analyzer (NanoString Technologies) was used to scan the cartridges at maximum resolution (555 fields of view), count individual fluorescent barcodes, and quantify the RNA molecules. Nanostring nSolver 4.0 software (NanoString Technologies) and "NanoStringNorm" package in R were used to control and normalize raw data. Data were first normalized against the geometric mean of 20 housekeeping genes. To control for technical sources of variability, data were also normalized against the geometric mean of six synthetic positive control targets. These gene expression values were then $\log_2$-transformed. Gene sets to investigate gene expression levels of various immune pathway signatures and immune cell subsets were established based on gene annotations of the nCounter PanCancer IO 360 Panel, giving a cell type profiling score.

Gene Set Enrichment Analysis (GSEA)

Gene Set Enrichment Analysis of RNAseq or ATACseq data was performed using fgsea, and genes were ranked by $\log_2$ fold-change statistic value (DESeq2). Normalized enrichment scores (NES) were calculated using Molecular Signatures Database (MSigDB) entries.

Statistical analyses

Statistical analyses were conducted using Prism software v7.3 (GraphPad Software, La Jolla, CA, USA). For *in vitro* and *in vivo* experiments, results are indicated as the mean ± SEM (SEM). For statistical testing of significance, ANOVA was used with the Tukey multiple comparisons test, with p values of *<0.05, **<0.01, ***<0.005, and ****<0.001. Mouse survival curves were evaluated using the log rank test to determine significance. All data shown in all figure panels, including H&E staining and IHC images, are representative of at least 3 independent experiments.